

2011

An Investigation of Two Ceramic Electron Conductors for Use in Solid Oxide Fuel Cell Anodes

Ian Hasson
Bucknell University

Follow this and additional works at: https://digitalcommons.bucknell.edu/masters_theses



Part of the [Chemical Engineering Commons](#)

Recommended Citation

Hasson, Ian, "An Investigation of Two Ceramic Electron Conductors for Use in Solid Oxide Fuel Cell Anodes" (2011). *Master's Theses*. 22.
https://digitalcommons.bucknell.edu/masters_theses/22

This Masters Thesis is brought to you for free and open access by the Student Theses at Bucknell Digital Commons. It has been accepted for inclusion in Master's Theses by an authorized administrator of Bucknell Digital Commons. For more information, please contact dcadmin@bucknell.edu.

I, Ian Hasson, do grant permission for my thesis to be copied.

AN INVESTIGATION OF TWO CERAMIC ELECTRON CONDUCTORS FOR USE
IN SOLID OXIDE FUEL CELL ANODES

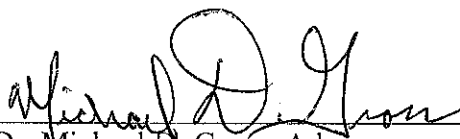
by

Ian D. Hasson

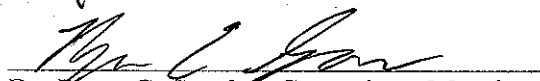
A Thesis

Presented to the Faculty of
Bucknell University
In Partial Fulfillment of the Requirements for the Degree of
Master of Science in Chemical Engineering


Approved:




Dr. Michael D. Gross, Advisor



Dr. Ryan C. Snyder, Committee Member



Dr. Katsuyuki Wakabayashi, Committee Member



Dr. Jeffrey Csernica, Department Chair

4-28-2011
Date

Acknowledgements

I would like to begin by thanking my advisor Dr. Michael D. Gross for without his support and guidance none of this would have been possible. I would also like to thank Brandon Smith and Kristin Bretscher, who worked in Dr. Gross' research group before me, for teaching me many of the skills necessary to complete this work. I want to also acknowledge the following students for working on this project with me at various points over these last two years: Tommy Lyons, Billy Holler, Amanda Britton, and Brian Harding.

Rainer Kungas and Dr. Ray Gorte at the University of Pennsylvania deserve many thanks for graciously opening their lab to me and teaching me many new techniques. I would like to thank Diane Hall, the Bucknell Chemical Engineering Laboratory Technician, for always keeping me in stock of necessary materials and Brad Jordan, the Bucknell Geology Lab Director, for letting me use the geology department's XRD.

My friends, both on campus and off, also deserve many thanks for making my time in graduate school a blast.

Lastly, I would like to thank my parents, David and Elizabeth, and my brother James, for their unwavering support as I pursued this thesis.

Table of Contents

Chapter 1 Introduction.....	1
1.1 Background.....	1
1.1.1 Solid Oxide Fuel Cell Operating Principles.....	1
1.1.2 Unique Solid Oxide Fuel Cell Advantages.....	2
1.1.3 The Anode Active Region.....	3
1.1.4 Limitations of a Ni Anode.....	4
1.2 Motivation.....	5
1.3 Thesis Outline.....	6
1.4 References.....	7
Chapter 2 Materials and Methods.....	10
2.1 Fabrication Methods for LSCM Study.....	10
2.1.1 Dense Slurry Manufacturing.....	10
2.1.2 Porous Slurry Manufacturing.....	11
2.1.3 Dual Tape Casting.....	12
2.1.4 Anode Lamination.....	13
2.1.5 Anode Infiltration.....	14

2.1.6	Anode Co-Sintering.....	15
2.1.7	Cathode Infiltration.....	16
2.1.8	Catalyst Infiltration into Anode.....	16
2.2	LSV Study Fabrication Methods.....	17
2.2.1	Dense Slurry Manufacturing.....	17
2.2.2	Porous Slurry Manufacturing.....	18
2.2.3	Assembling the Cell.....	19
2.2.4	Infiltrating the Electrodes.....	20
2.2.5	Porous Slabs.....	20
2.2.6	Powder Samples.....	21
2.3	Electrochemical Testing.....	22
2.3.1	Cell Testing Preparation.....	22
2.3.2	Flow System.....	23
2.3.3	V-i Curve.....	24
2.3.4	Electrochemical Impedance Spectroscopy.....	25
2.3.5	Conductivity Testing.....	27
2.4	Phase and Microstructure Measuring Techniques.....	29
2.4.1	Powder X-ray Diffraction.....	29

2.4.2	Thermal Gravimetric Analysis	30
2.4.3	BET Isotherm	30
2.5	References.....	32
Chapter 3 Effect of Microstructure on Anode Catalytic Performance for Co-Sintered and Infiltrated LSCM		33
3.1	Introduction.....	33
3.1.1	Effectiveness of Pd in Co-sintered and Infiltrated Cells	33
3.2	The Effect of Fabrication Method on Microstructure.....	35
3.3	Experimental	38
3.4	Results.....	40
3.5	Conclusions.....	43
3.6	References.....	44
Chapter 4 Investigation of LSV for use as a Potential Electron Conductor in SOFC Anodes.....		45
4.1	Introduction.....	45
4.1.1	Motivation	45
4.2	Experimental	46
4.3	Results.....	48
4.3.1	Powder X-ray Diffraction of various LSV compositions.....	48

4.3.2	Thermal Gravimetric Analysis	50
4.3.3	Analyzing the Anode Microstructure with SEM and BET Isotherm	51
4.3.4	Conductivity of LSV samples	53
4.3.5	Cell Testing	54
4.3.6	Vanadium Deficient Optimization	60
4.3.7	TGA of Vanadium Deficient LSV	61
4.3.8	Conductivity of Vanadium Deficient Slabs	62
4.4	Conclusions.....	64
4.5	Future Work.....	65
4.6	References.....	66

List of Tables

Table 3.1 Anode Configurations for Fuel Cell Testing.	38
Table 4.1 Specific surface areas of LSV-YSZ composites fabricated at 973 K or 1373 K, before and after reduction.	53
Table 4.2 Maximum power densities of the cells at 973 K in humidified H ₂ , with anode having 10 vol-% LSV, together with Pd and ceria. In these experiments, the vanadium content of the LSV phase (La _{0.7} Sr _{0.3} V _{1+δ} O _{2.85}) was varied and the cells were heated to 973 K in air before reduction to study the effect of interactions between the LSV phase and the Pd/ceria catalyst.	59

List of Figures

Figure 1.1 Solid Oxide Fuel Cell Schematic utilizing Hydrogen and Oxygen with half reactions. ³	2
Figure 1.2 Diagram of Active Region in SOFC Anode. ⁴	3
Figure 2.1 Schematic of Dual Tape Casting. ¹	13
Figure 2.2 Schematic of Laminating Electrodes to Electrolyte. ¹	14
Figure 2.3 Schematic of fuel cell bonded to alumina tube. ¹	22
Figure 2.4 Schematic of Flow Control System.	23
Figure 2.5 V-i and P-i curves for infiltrated LSCM-YSZ anodes with Pd catalyst at 923K in Humidified H ₂ . (~3% H ₂ O)	24
Figure 2.6 Electrical impedance spectroscopy technique. ¹	26
Figure 2.7 Real versus Imaginary impedance showing ohmic and non-ohmic losses. ¹ ..	26
Figure 2.8 Diagram of a Slab Ready for Conductivity Testing.	28
Figure 3.1 Cell performance curves for LSCM-YSZ anodes without Pd catalyst (circles) and with infiltrated Pd catalyst (triangles) in humidified H ₂ (3% H ₂ O). a) LSCM-YSZ co-sintered at 1473 K in air ⁴ b) YSZ sintered at 1823 K in air followed by infiltration of LSCM and calcination at 1473 K in air. ⁵	34
Figure 3.2 Schematic of a) a Ni-YSZ anode and b) a YSZ anode with separate e ⁻ ceramic conductor and catalyst.	35
Figure 3.3 Schematic of a) a co-sintered ceramic conductor/YSZ anode with an infiltrated catalyst and b) a sintered YSZ anode with infiltrated ceramic conductor and catalyst.	36
Figure 3.4 Comparing cell performance of ‘A’ LSCM-YSZ co-sintered anode with and without Pd catalyst (black squares and white squares respectively) and ‘B’ LSCM-YSZ Infiltrated anode with and without Pd catalyst (black triangles and white triangles respectively) at 973K in Humidified H ₂	40
Figure 4.1 XRD patterns of varying compositions of La _{1-x} Sr _x VO ₃ with a) Post redox cycle, oxidation in air and reduction in H ₂ both at 700°C for 10 hours b) Reduced in H ₂ at 1400°C for 10 hours c) LaVO ₃ standard pattern.	49

Figure 4.2 TGA curves for the reduction of $\text{La}_{0.7}\text{Sr}_{0.3}\text{VO}_{3.85}$ in 4% H_2/Ar and oxidation of $\text{La}_{0.7}\text{Sr}_{0.3}\text{VO}_{2.85}$.	50
Figure 4.3 SEM images of (a) the initial YSZ scaffold. The LSV-YSZ composite calcined at 973 K (b) before and (c) after reduction. The LSV-YSZ composite calcined at 1373 K (d) before and (e) after reduction.	52
Figure 4.4 Conductivity data for LSV bulk pellet reduced in H_2 at 1773 for 10hrs (squares) and LSV-YSZ composite calcined at 973 k for 10 hours and then reduced during testing (triangles).	54
Figure 4.5 $V-i$ polarization curves and impedance spectra of cells at 973 K using LSV-YSZ anode with (■) and without (●) CeO_2 and Pd. Data for the LSCM-YSZ anode with CeO_2 and Pd (▲). ⁵	56
Figure 4.6 $V-i$ polarization curves and impedance spectra of cell having LSV-YSZ anode with CeO_2 and Pd in humidified (3% H_2O) H_2 (■) or CH_4 (▲) at 1073 K. ⁵	57
Figure 4.7 $V-i$ polarization curves in humidified (3% H_2O) H_2 for cells having LSV-YSZ anodes with Pd/ceria catalysts. Data are shown before (■) and after (▲) heating the composite to 973 K in air. ⁵	58
Figure 4.8 XRD plot of varying compositions of $\text{La}_{0.7}\text{Sr}_{0.3}\text{V}_x\text{O}_3$ sintered in Air at 973K for 10hr and reduced in H_2 at 973K for 10hr.	61
Figure 4.9 TGA curves for the reduction of $\text{La}_{0.7}\text{Sr}_{0.3}\text{V}_x\text{O}_3$ in 5% $\text{H}_2/95\%\text{Ar}$ Conductivity of Vanadium Deficient LSV.	62
Figure 4.10 Conductivity data of various compositions of $\text{La}_{0.7}\text{Sr}_{0.3}\text{V}_y\text{O}_3$, $x = 1.0$ (diamonds), $x = 0.95$ (squares), $x = 0.9$ (triangles).	63

Abstract

AN INVESTIGATION OF TWO CERAMIC ELECTRON CONDUCTORS FOR USE
IN SOLID OXIDE FUEL CELL ANODES

Ian D. Hasson

Dr. Michael D. Gross (Advisor)

Solid oxide fuel cells (SOFCs), a particular type of fuel cell, are a promising power generation technology, however further research is required before they will be considered for the industrial scale. The unique advantages that differentiate SOFCs from other types of fuel cells are not being realized because of limitations created by the current anode material, Ni. This thesis conducted work with two potential alternatives to Ni, $\text{La}_{0.8}\text{Sr}_{0.2}\text{Cr}_{0.5}\text{Mn}_{0.5}$ (LSCM) and Sr doped LaVO_3 (LSV) to serve as the electron conductor in the anode of SOFCs.

LSCM has already been identified as a good electron conductor and suitable for use in SOFC anodes. LSCM lacks the catalytic ability to serve as an oxidation catalyst therefore an additional catalyst must be added to the anode. Two literature sources using a co-sintered and an infiltrated LSCM anode reported contradicting conclusions concerning the effectiveness of Pd as an oxidation catalyst with LSCM. In order to verify and further explore these findings, fuel cells with identical compositions were constructed using both the co-sintered and infiltrated methods for performance testing. Contrary to

the literature, it was found that the addition of Pd resulted in a significant improvement of cell performance for both the co-sintered and infiltrated cells.

LSV, a relatively new material, has shown extremely high conductivity but has not been extensively studied in fuel cell applications. In order to assess this novel material, fundamental characterization tests such as powder x-ray diffraction, conductivity, thermal gravimetric analysis, and BET isotherm tests as well as initial fuel cell performance tests were conducted. It was found that LSV maintains a single phase after initial reduction and after a redox cycle at a maximum Sr doping concentration of $\text{La}_{0.6}\text{Sr}_{0.4}\text{VO}_3$. Good conductivity was achieved in both infiltrated porous slabs and bulk pellet conductivity tests. Fuel cell tests were also conducted and LSV achieved good performance in both humidified H_2 and CH_4 with an additional oxidation catalyst. Significant performance losses were noted when the anode was exposed to Air at high temperatures after the addition of the oxidation catalyst. Further tests found that this performance loss could be minimized if the LSV was made to be vanadium deficient indicating there may be some negative interaction between the vanadium and the Pd catalyst.

Chapter 1 Introduction

1.1 Background

Fuel cells are energy conversion devices that directly convert chemical energy into electrical energy. Although fuel cells are not strictly a renewable energy technology, they are often included in this category due to significant advantages over traditional power generation devices. The major advantages of fuel cells include 1) high efficiencies 2) low emissions 3) simple scalability to meet a wide variety of power requirements, and 4) low noise pollution.^{1,2}

1.1.1 Solid Oxide Fuel Cell Operating Principles

There are many types of fuel cells, which are primarily distinguished by their material of construction. This thesis concentrates solely on one type of fuel cell, the solid oxide fuel cell (SOFC). The SOFC electrolyte contains a dense solid metal oxide, which is how the name of this fuel cell was derived. Like all electrochemical cells, a SOFC is comprised of an electrolyte, an anode, and a cathode. A diagram of a SOFC with half reactions utilizing hydrogen as fuel is shown in Figure 1.1. SOFCs utilize a yttrium stabilized zirconium (YSZ) electrolyte to transport oxygen ions between the cathode and anode. The electrolyte is also an electron insulator, forcing the electrons generated at the anode to flow through an external circuit, which can be used to satisfy a load. The oxidation reaction occurs at the anode, also known as the fuel electrode and the reduction reaction occurs at the cathode, also known as the air electrode.

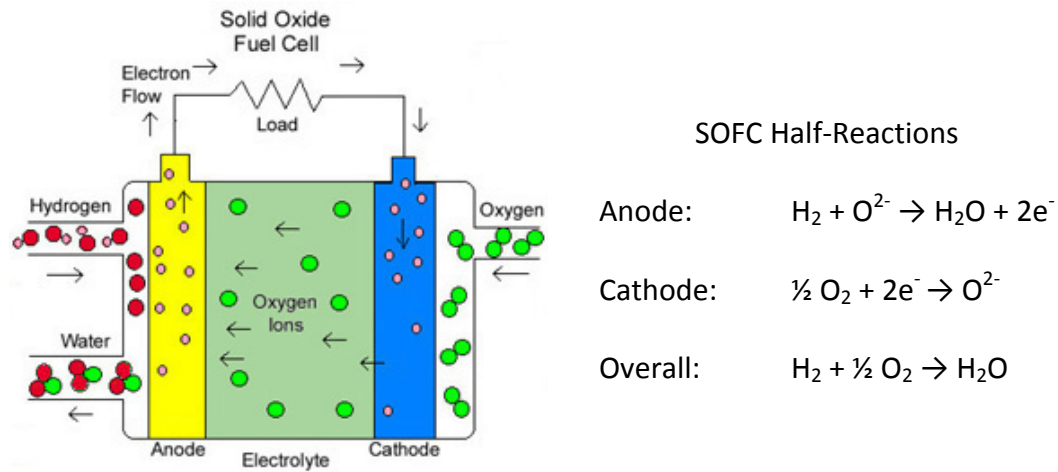


Figure 1.1 Solid Oxide Fuel Cell Schematic utilizing Hydrogen and Oxygen with half reactions.³

1.1.2 Unique Solid Oxide Fuel Cell Advantages

SOFCs have two major advantages over other types of fuel cells. First, SOFCs have a higher efficiency than other fuel cells. The department of energy has shown that a cogeneration SOFC power generation system could have efficiencies upward of 90%.² SOFCs operate at high temperatures, 600-1000°C, in order to achieve reasonable ionic conductivity (0.02-0.1 S/cm²) through the YSZ electrolyte.¹ The high operating temperatures make SOFCs ideal for stationary cogeneration power because cogeneration power systems recycle the excess heat produced during power generation for increased overall efficiency. Second, SOFCs can theoretically operate on any oxidizable fuel, including but not limited to H₂, CO, hydrocarbons and alcohols. No other type of fuel cell has the wide range of fuel flexibility available to SOFCs. Other fuel cells are limited to

running exclusively on hydrogen and therefore must first reform fuels like hydrocarbons to H_2 , significantly reducing the overall efficiency of the fuel cell system.¹

Our research group considers the fuel flexibility advantage of SOFCs to be critical to the future success of SOFCs. Therefore my research has focused exclusively on the fuel electrode, the anode.

1.1.3 The Anode Active Region

In SOFC anodes, the most important area is the active region, which is the region where the anode half reaction occurs. The active region begins at the anode/electrolyte interface and goes approximately $10\mu m$ into the anode. Figure 1.2 is a two dimensional representation of the active region in the anode of an SOFC.

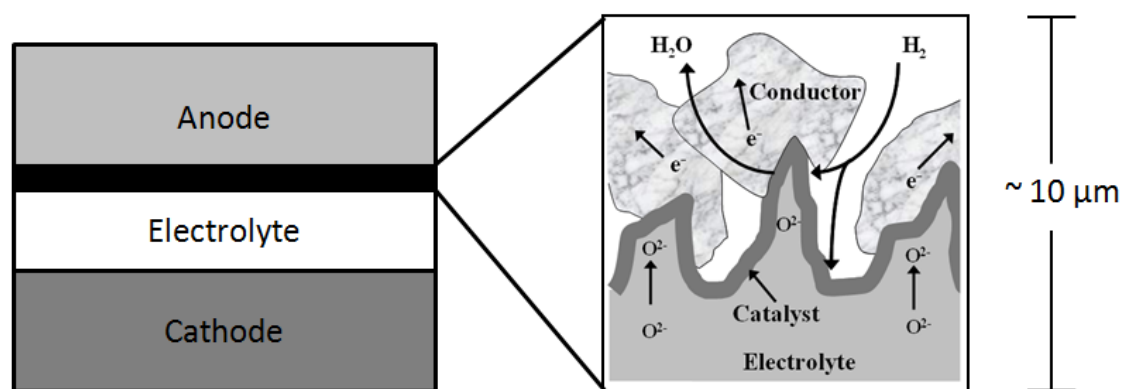


Figure 1.2 Diagram of Active Region in SOFC Anode.⁴

In order for a fuel cell to operate, four processes must occur in the active region: 1) the fuel must diffuse through the porous anode to the active region, 2) the oxygen ions generated from the cathode must reach the active region, 3) a catalyst must be present for the required oxidation reaction to occur, and 4) electrons generated by the reaction must

conduct through the anode to an external circuit. The most developed SOFCs anodes are constructed from a porous composite of YSZ and Ni, where Ni serves as both the electron conductor and oxidation catalyst.⁶ Ni, however, has many limitations which are preventing SOFCs from reaching their full potential.

1.1.4 Limitations of a Ni Anode

Using Ni in the anode eliminates many potential fuel options. Ni is only able to operate on syngas, a mixture of H₂ and CO, or methane when co-fed with significant amounts of steam, and is unable to operate on larger hydrocarbons.^{6, 7} In the presence of larger hydrocarbons, Ni catalyzes the formation of carbon fibers, resulting in mechanical fracture of the cell.⁸⁻¹⁴ Also, sulfur poisons the catalytic activity of nickel resulting in significant performance losses at sulfur concentrations less than 1 ppm.¹⁵ Therefore, any fuel sent to a Ni SOFC must be thoroughly scrubbed prior to entering the anode, further increasing the operating cost. Finally, Ni is not stable during cycles of reduction and oxidation (redox cycling) due to the expansion that occurs when Ni oxidizes to NiO.^{16, 17} Ni is a very good oxidation catalyst and electron conductor however the lack of fuel flexibility cripples the scope of applications available for SOFCs.

1.2 Motivation

The ultimate goal of my work is to explore alternative materials to replace Ni. Other metals are not suitable for SOFCs because they are either not fuel flexible like Ni or exhibit very poor thermal stability. For example, Cu easily sinters at the high SOFC operating temperatures preventing it from being a good electron conductor in SOFC applications.^{18, 19} Precious metals, such as Pt, are fuel flexible and thermally stable; however, the cost of Pt is simply too high.

One potential replacement for Ni is metal oxides (ceramics). Ceramic materials have been shown to be stable in a wide variety of carbon containing fuels and have good thermal stability. However, it is difficult for metal oxides to have good electron conductivity and catalytic activity for the oxidation reaction.²⁰⁻²²

One solution is to use two separate materials for the electron conductor and catalyst. By separating the catalyst previously unavailable materials such as precious metals may now be utilized because the catalyst is present at a much lower loading than the electron conductor. Separating the catalyst allows us to narrow our search to metal oxides that are good electron conductors. $\text{La}_{0.8}\text{Sr}_{0.2}\text{Cr}_{0.5}\text{Mn}_{0.5}$ (LSCM) and $\text{La}_{1-x}\text{Sr}_x\text{VO}_3$ (LSV) have been identified as good candidates and have exhibited bulk conductivities of 1 S/cm and 100 S/cm respectively.²³⁻²⁵

1.3 Thesis Outline

This thesis includes two separate investigations involving LSCM and LSV. LSCM has been shown to exhibit good conductivity and fuel cell performance. However, the literature presents conflicting conclusions concerning the impact of LSCM anode microstructure on catalyst effectiveness.^{8, 26} This project sought to first reproduce the literature data and then expand on it believing that the microstructure was determining the effectiveness of the catalyst within the anode.

The second project involves exploring LSV, as a potential electron conductor in SOFCs. LSV has shown extremely high conductivity but has not been extensively studied in fuel cell applications. In this project we completed fundamental material characterization tests such as powder x-ray diffraction, conductivity, thermal gravimetric analysis, and BET Isotherm tests. Initial studies on fuel cell performance were also completed.

The remainder of this thesis is laid out as follows: Chapter 2 describes general fabrication methods utilized in both of the LSCM and LSV projects. Chapter 3 contains the results for the investigation into the LSCM microstructure. Chapter 4 contains the results from the fundamental characterization of LSV and initial fuel cell performance tests.

1.4 References

1. Larminie, J. D. *Fuel Cell Systems Explained*, New Jersey: Wiley & Sons Ltd, 2003.
2. Comparison of Fuel Cell Technologies. http://www1.eere.energy.gov/hydrogenandfuelcells/fuelcells/pdfs/fc_comparison_chart.pdf. (accessed Jan 23, 2010)
3. Solid Oxide Fuel Cell SOFC: Concurrent Technology. http://www.fctec.com/fctec_types_softc.asp. (accessed Feb 1, 2010)
4. Gross, M.D. PhD Dissertation, University of Pennsylvania; **2007**.
5. Simner, S.P.; Bonnett, J.F.; Canfield, K.D.; Mienhardt, V.L.; Sprenkle, V.L.; Stevenson, J.W. Optimized Lanthanum Ferrite-Based Cathodes for Anode Supported SOFCs. *Electrochemical and Solid-State Letters*. **2002**, A173-A175.
6. Singhal, S.C. Solid Oxide Fuel Cells: Status, Challenges and Opportunities. *Advances in Science and Technology*. **2006**, 45, 1837-1846.
7. Cimenti, M.; Hill, J.M.; Direct Utilization of Liquid Fuels in SOFC for Portable Applications: Challenges for the Selection of Alternative Anodes. *Energies*. **2009**, 2, 377-410.
8. Kim, G.; Corre, G.; Irvine, J. T. S.; Vohs, J. M.; Gorte, R. J.; Engineering Composite Oxide SOFC Anodes for Efficient Oxidation of Methane. *Electrochemical and Solid-State Letters*. **2008**, B16-B19.
9. Takeguchi, T.; Kani, Y.; Yano, T.; Kikuchi, R.; Eguchi, K.; Tsujimoto, K.; Uchida, Y.; Ueno, A.; Omoshiki, K.; Aizawa, M.; Study on Steam Reforming of CH₄ and C₂ Hydrocarbons and Carbon Deposition on Ni-YSZ Cermets. *Journal of Power Sources*. **2002**, 588-595.
10. McIntosh, S. G. Direct Hydrocarbon Solid Oxide Fuel Cells. *Chemical Reviews*. **2004**, 104, 4845-65.
11. Kim, H.; Lu, C.; Worrell, W.; Vohs, J.; Gorte, R. Cu-Ni Cermet Anodes for Direct Oxidation of Methane in Solid-Oxide Fuel Cells. *Journal of Electrochemical Society*. **2002**, A247-A250.

12. Toebes, M.L.; Bitter, J.H.; Van Dillen, A.J.; de Jong, K.P. Impact of the Structure and Reactivity of Nickel Particles on the Catalytic Growth of Carbon Nanofibers. *Catalysis Today*. **2002**, 76, 33-42.
13. Sun, C.; Stimming, U. Recent Anode Advances in Solid Oxide Fuel Cells. *Journal of Power Sources*. **2007**, 171, 247-260.
14. Helveg, S.; López-Cartes, C.; Sehested, J.; Hansen, P.L.; Clausen, B.S.; Rostrup-Nielsen, J.R.; Abild-Pedersen, F.; Nørskov, J.K. Atomic-scale Imaging of Carbon Nanofibre Growth. *Nature*. **2004**, 427, 426-429.
15. Nagel, F.P.; Schildhauer, T.J.; Sfeir, J.; Schuler, A.; Biollaz, S.M.A. The Impact of Sulfur on the Performance of a Solid Oxide Fuel Cell (SOFC) System Operated with Hydrocarbonaceous Fuel Gas. *J Power Sources*. **2009**, 189, 1127-1131.
16. Stathis, G.; Simwonis, D.; Tietz, F.; Moropoulou, A.; Naoumides, A. Oxidation and Resulting Mechanical Properties of Ni/8Y₂O₃-Stabilized Zirconia Anode Substrate for Solid-Oxide Fuel Cells. *Journal of Materials Research*. **2002**, 17, 951-958.
17. Cassidy, M.; Lindsay, G.; Kendall, K. The Reduction of Nickel-Zirconia Cermet Anodes and the Effects on Supported Thin Electrolytes. *Journal of Power Sources*. **1996**, 61, 189-192.
18. Jung, S.; Lu, C.; He, H.; Ahn, K.; Gorte, R.J.; Vohs, J.M. Influence of Composition and Cu Impregnation Method on the Performance of Cu/CeO₂/YSZ SOFC Anodes. *Journal of Power Sources*. **2006**, 154, 42-50.
19. Gross, M.D.; Vohs, J.M.; Gorte, R.J. A Study of Thermal Stability and Methane Tolerance of Cu-based SOFC Anodes with Electrodeposited Co. *Electrochimica Acta*. **2007**, 52, 1951-1957.
20. Atkinson, A.; Barnett, S.; Gorte, R.J.; Irvine, J. T. S.; McEvoy, A.J.; Mogensen, M.; Singhal, S.C.; Vohs, J. Advanced Anodes for High-Temperature Fuel Cells. *Nature Materials*. **2004**, 3, 17-27.
21. Gorte, R.J.; Vohs, J.M. Novel SOFC Anodes for the Direct Electrochemical Oxidation of Hydrocarbons. *Journal of Catalysis*. **2003**, 216, 477-486.
22. Park, S.; Gorte, R.J.; Vohs, J.M. Applications of Heterogeneous Catalysis in the Direct Oxidation of Hydrocarbons in a Solid-Oxide Fuel Cell. *Applied Catalysis* **2000**, 200, 55-61.

23. Tao, S.; Irvine, J.T.S. Synthesis and Characterization of $(\text{La}_{0.75}\text{Sr}_{0.25}\text{Cr}_{0.5}\text{Mn}_{0.5}\text{O}_{3-\delta})$, a Redox-Stable, Efficient Perovskite Anode for SOFCs. *Journal of Electrochemical Society*. **2004**, 151, 252-259.
24. Ge, X.; Chan, S. Lanthanum Strontium Vanadate as Potential Anodes for Solid Oxide Fuel Cells. *Journal of Electrochemical Society*. **2009**, 156, B386-B391.
25. Cheng, Z.; Zha, S.; Aguilar, L.; Liu, M. Chemical, Electrical, and Thermal Properties of Strontium Doped Lanthanum Vanadate. *Solid State Ionics*. **2005**, 176, 1921-1928.
26. Jiang, S.P.; Ye, Y.; He, T.; Ho, S.B. Nanostructured Palladium- $\text{La}_{0.75}\text{Sr}_{0.25}\text{Cr}_{0.5}\text{Mn}_{0.5}\text{O}_3/\text{Y}_2\text{O}_3\text{-ZrO}_2$ Composite Anodes for Direct Methane and Ethanol Solid Oxide Fuel Cells. *Journal of Power Sources*. **2008**, 185, 179-182.

Chapter 2 Materials and Methods

2.1 Fabrication Methods for LSCM Study

2.1.1 Dense Slurry Manufacturing

In order to create a fuel cell, one must first make slurries which can be tape casted into the desired fuel cell components (anode, cathode, and electrolyte). Electrolytes were constructed from dense YSZ slurry, meaning that this slurry does not contain pore formers. In the LSCM study, the recipe for the dense electrolyte slurry was as follows:

40 g YSZ (Tosh, TZ-8Y)

18 mL DI-H₂O

1.07 g D-3005 (dispersant, Duramax)

9.6 g HA-12 (binder, Duramax)

14.4 g B-1000 (binder, Duramax)

0.5 g Triton X-1000 (dispersant, MP Biomedicals)

Constructing the dense slurry begins by combining the YSZ, de-ionized water, and D-3005 into a polyethylene bottle with YSZ grinding media (5 mm diameter spherical particles 5 mol% Y₂O₃, 95 mol% ZrO₂). The mixture was ball milled for 24 hours to ensure thorough mixing. Once the slurry was separated from the grinding media, the binders HA-12 and B-1000 as well as the dispersant Triton X-1000 were added. The

slurry was magnetically stirred and left open to the atmosphere to dry. The actual time of drying was dependent upon the slurry and was determined qualitatively, by placing a drop of slurry on the hydrophobic side of a mylar film. The slurry was finished drying when a drop of slurry did not bead up on the hydrophobic mylar tape. After drying to an appropriate level the slurry was ready for tape casting.

2.1.2 Porous Slurry Manufacturing

As opposed to the electrolyte, the electrodes require porosity. Therefore, the electrode slurries contained YSZ and pore formers. For the LSCM project, the porous electrode slurries were made with the following recipe:

40 g YSZ (Tosh, TZ-8Y)

18 mL DI-H₂O

1.07 g D-3005 (dispersant, Duramax)

9.6 g HA-12 (binder, Duramax)

14.4 g B-1000 (binder, Duramax)

0.5 g Triton X-1000 (binder, MP Biomedicals)

18.3 g Pore former

Similar to the electrolyte slurry, the electrode slurry begins by combining the YSZ, de-ionized water, D-3005, and the pore former of choice in a polyethylene bottle with YSZ grinding media (5mm diameter spherical particles 5 mol% Y₂O₃, 95 mol%

ZrO₂). The term pore former is kept general here since different pore formers can be utilized to achieve a desired pore size and morphology in the electrode. In this thesis, the cathode slurry was constructed with 7.8g of graphite (Alfa Aesar) and 10.5g of poly(styrene-co-divinylbenzene) (Aldrich) and the anode slurry was constructed with 18.3g of graphite (Alfa Aesar). The solution was ball milled for 24 hours to ensure thorough mixing. Once mixed, the slurry was separated from the grinding media and the binders HA-12 and B-1000 as well as the dispersant Triton X-1000 were added to the slurry. The slurry was magnetically stirred and left open to the atmosphere to dry until an appropriate amount of water had evaporated from the solution, at which time the slurry was ready for tape casting.

2.1.3 Dual Tape Casting

There are two methods available for combining the porous electrode components and the dense electrolyte components into a complete fuel cell. One may either cast the electrode slurry directly onto the electrolyte, a method known as dual tape casting, or the electrode and electrolyte tapes may be cast separately and then combined, a method known as lamination. The following sections will describe these two methods.

In dual tape casting the electrode is tape casted directly onto the already casted electrolyte film, shown in Figure 2.1. First the electrolyte slurry (white) is poured onto the hydrophobic side of a mylar carrier film. A doctor blade is then drawn across the film ensuring an even thickness to the film. Once the electrolyte slurry has dried the electrode slurry (grey) is poured directly onto the electrolyte. Again a doctor blade is utilized to

ensure an even thickness of the electrode film. Once the electrode slurry dries the cell may be punched out of the tape using a 2.5 cm diameter circular punch.

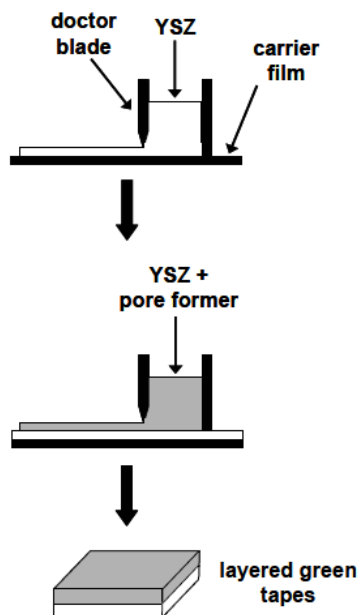


Figure 2.1 Schematic of Dual Tape Casting. ¹

Dual tape casting ensures better adherence between the electrode and the electrolyte, however it is very difficult to do with a thin electrode, less than 50 μm .¹ Dual tape casting was used to attach all cathodes in the LSCM study. The anodes were attached by lamination (section 2.1.4) or by co-sintering (section 2.1.6).

2.1.4 Anode Lamination

LSCM anodes were created by the lamination method, shown in Figure 2.2. When laminating the electrolyte and electrode, slurries were tape-casted separately onto the hydrophobic side of mylar tape, punched out separately with 2.5 cm and 1 cm diameter punches respectively, and then pressed together in a heated laboratory press.

Lamination is more suitable for thin electrodes but is more difficult to execute due to the risk of cell fracture, if pressed too forcefully, or poor adhesion, if not pressed evenly across the cell.¹ Once attached the cell is heated to 1823 K for 5 hours, to sinter the cell.

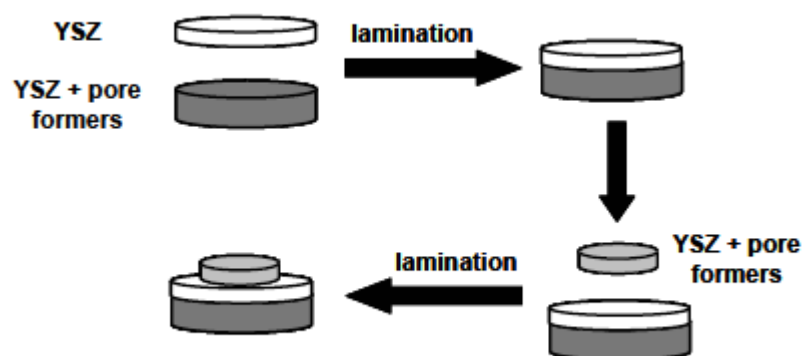


Figure 2.2 Schematic of Laminating Electrodes to Electrolyte.¹

2.1.5 Anode Infiltration

Up to this point the anode is only made of porous YSZ. The electron conductor must be infiltrated into the anode, separately. Infiltration involves creating a precursor solution of salts, which is dropped onto the porous electrode. The LSCM infiltration solution was prepared by combining stoichiometric amounts of $\text{La}(\text{NO}_3)_3 \cdot 6\text{H}_2\text{O}$ (99.9%, Alfa Aesar), $\text{Sr}(\text{NO}_3)_2$ (99.9%, Alfa Aesar), $\text{Cr}(\text{NO}_3)_3 \cdot 9\text{H}_2\text{O}$, $(\text{CH}_3\text{COO})_2\text{Mn} \cdot 4\text{H}_2\text{O}$, and citric acid in de-ionized water to a concentration of 0.7 M. The solution was infiltrated into the porous electrode and then the cell was heated to 723 K in order to vaporize the nitrate salts. This process was repeated until the desired loading was reached, which was determined by measuring the cells change in mass. Once the desired loading was achieved the cells were heated in air to 1473 K to form the desired metal oxide.

2.1.6 Anode Co-Sintering

Another more traditional method of anode construction known as co-sintering was also used in the LSCM study. In co-sintering, the YSZ, LSCM, and pore former are mixed together and then painted onto the electrolyte. The cell was then heated and the pore former was burned out of the anode, leaving a porous structure.

In order to prepare a co-sintered anode, LSCM powders were first created. LSCM powders were created by combining stoichiometric amounts of Cr_2O_3 , MnO_2 , SrCO_3 , and La_2O_3 in an ethanol solution and ball milling with YSZ grinding media for 12 hours. After milling, the solution is dried to remove the solvent, ground with a mortar and pestle, and then calcined at 1473 K for 10 hours. After calcination, the LSCM reagents were combined again with ethanol and YSZ grinding media and milled for another 12 hours. The solution was dried again in a drying oven to remove the ethanol. After this final drying step the LSCM powder was ready to make a co-sintered anode.

The previously described LSCM powder, YSZ and a pore former were combined with ethanol and ball milled for 24 hours. After milling, the solution was dried in an oven for 24 hours. The resulting dried solid was ground into a fine powder with a mortar and pestle. The fine powder was mixed with glycerin until a thick paste was formed. The paste was painted onto the electrolyte using a stencil as a guide to ensure proper geometry and thickness of the anode. After painting, the cell was sintered at 1473 K for 2 hours. The high temperature step burns out the pore former leaving a porous anode of co-sintered LSCM and YSZ.

2.1.7 Cathode Infiltration

$\text{La}_{0.7}\text{Sr}_{0.3}\text{FeO}_3$ (LSF) is the material of choice for the cathode because it has a high conductivity and catalytic activity for the reduction of oxygen at relatively low operating temperatures (973K-1073K).² In order to complete the cathode, LSF was infiltrated into the porous structure.

For the cathode infiltrations, a 0.7M LSF solution was utilized. The LSF solution was created by combining stoichiometric amounts of $\text{La}(\text{NO}_3)_3 \cdot 6\text{H}_2\text{O}$, $\text{Sr}(\text{NO}_3)_2$, $\text{Fe}(\text{NO}_3)_3 \cdot 9\text{H}_2\text{O}$, and citric acid with de-ionized water. The solution was then dropped onto the porous cathode and subsequently the cell was heated to 723 K to decompose the nitrate salts, leaving only the desired components. Infiltration was utilized because it allows for percolation at lower loadings than a random mixture.³ Once a desired loading is reached the electrode is heated to 1123 K for 4 hours to form the desired oxide.

2.1.8 Catalyst Infiltration into Anode

A catalyst was added to the anode after all other components of the anode and cathode were constructed. The LSCM study utilized Pd as a catalyst which was added by infiltration of a Pd solution (0.45 M Tetraammine palladium (II) nitrate solution, Alfa Aesar, 99.9%). The Pd was infiltrated to a final loading of 0.5 wt%.

2.2 LSV Study Fabrication Methods

2.2.1 Dense Slurry Manufacturing

Similar to the LSCM cell fabrication technique, fabricating LSV anode cells begin by constructing dense electrolyte slurry for tape casting. The slurry for the LSV project utilized ethanol as the primary solvent as opposed to water, which was used in the LSCM project. The dense slurry was made from the following recipe:

40g YSZ powder (Tosh, TZ-8Y)
8.5g 200 Proof Ethanol (Pharmco Aaper)
10 g Xylenes Mixed (Alfa Aesar)
0.8g Blown Menhaden Fish Oil (TCW)
1.2 g Polyethylene Glycol (Alfa Aesar)
1.2 g Benzyl Butyl phthalate (TCW)
(Varying Amount) Polyvinyl Butyral B-98 (TCW)

150g of YSZ grinding media (5mm spherical particles 5 mol% Y₂O₃, 95 mol% ZrO₂), ethanol, mixed xylenes, and blown menhaden fish oil were added to a polyethylene bottle. This solution was milled for approximately 10 minutes, after which the YSZ was added. The solution was then milled for 12 hours. After milling, the polyethylene glycol and benzyl butyl phthalate were added and the bottle was shaken

vigorously for 5 minutes. After shaking, 12.75g of a binder solution was added. The binder solution was made by combining ethanol and polyvinyl butyral B-98 in a ratio of 17.5g of ethanol to 3g of Polyvinyl Butyral B-98 in a polyethylene bottle. This binder solution must be milled for 12 hours prior to use and then continuously milled when not in use. It is recommended that a large batch (approximately 60g worth) of binder solution be made. Once the binder solution was added the slurry was milled for another 12 hours before casting.

2.2.2 Porous Slurry Manufacturing

Again the electrode required porosity so a porous slurry was constructed. The electrode slurry was constructed from the following recipe:

40 g YSZ powder (Tosh, TZ-8Y)
12.6 g 200 Proof Ethanol (Pharmco Aaper)
50.3 g Xylenes Mixed (Alfa Aesar)
0.9 g Blown Menhaden Fish Oil (TCW)
16.2 g Polyvinyl Butyral B-79 (TCW)
(Varying Amount) Polyethylene Glycol (Alfa Aesar)
(Varying Amount) Benzyl Butyl phthalate (TCW)
(Varying Amount) Graphite (Alfa Aesar)

150g of YSZ grinding media, 0.9 g of fish oil, 12.6 g of 200 proof ethanol, and 50.3 g of mixed xylenes were added to a polyethylene bottle. The slurry was shaken vigorously before the addition of 40 g of YSZ and then milled for 12 hours. After milling 16.2 g of polyvinyl butyral B-79 were added and the slurry was milled for another 12 hours. The slurry was separated from the grinding media into two polyethylene sample bottles. For every 120g of slurry 6.95g of polyethylene glycol, 6.95g of benzyl butyl phthalate, and 30.6g of graphite were added. The slurry was manually well mixed before being returned to the ball mill without media. The slurry was milled for another 12 hours before casting. The electrode slurry may either be formed into a porous slab or casted to eventually create the fuel cell electrodes.

2.2.3 Assembling the Cell

For all the cells in the LSV study, the cathode and anode were attached to the electrolyte through lamination. The porous electrode was laminated as described previously in section 2.1.5. The dense and porous slurries were tape casted on two separate sheets of mylar film using a doctor blade to ensure an even thickness of the film. Once dried the dense film was punched out with a 2.5 cm diameter circular hole punch, while the porous film was punched out with a 1 cm circular diameter hole punch. Porous electrode film discs were then pressed onto either side of the dense electrolyte using a laboratory press. The cell was heated to 1823 K for 5 hours in order to sinter the cell.

2.2.4 Infiltrating the Electrodes

Since both the cathode and anode were assembled by lamination, both required infiltration. The LSV cathodes were infiltrated with the 0.7 M LSF solution using the same procedure described previously, in section 2.1.7.

For the LSV anode, 0.7 M aqueous solution of LSV was utilized which was created by combining stoichiometric amounts of $\text{La}(\text{NO}_3)_3 \cdot 6\text{H}_2\text{O}$ (99.9%, Alfa Aesar), $\text{Sr}(\text{NO}_3)_2$ (99.9%, Alfa Aesar), NH_4VO_3 (99.9%, Alfa Aesar), citric acid in de-ionized water. Before infiltrating, the solution was heated to 330 K for four hours. The aqueous solution was infiltrated into the anode and afterward heated to 723 K to vaporize the nitrate salts. The process of infiltration and heating to 723 K was repeated until the desired loading was reached. The final ceramic structure was formed once the anode underwent a final high temperature step at 973 K in air.

2.2.5 Porous Slabs

Porous slabs are used to imitate large porous YSZ anodes and were used for conductivity tests and BET isotherm tests. Porous slabs were formed by pouring the porous LSV slurry into molds and then cutting the dried slurry into rectangular blocks with dimensions of approximately 1 mm x 1 mm x 10 mm. These blocks were then sintered at 1823 K for 4 hours to form the final porous structure. Similar to the anodes, the porous slabs were then infiltrated with the previously described LSV solution (section 2.2.4) and again fired at 973 K once the final loading was reached.

2.2.6 Powder Samples

A bulk powder LSV samples were required to perform powder X-ray diffraction and bulk conductivity tests. Powder LSV samples were created by mixing stoichiometric amounts of La_2O_3 (Alfa Aesar), SrCO_3 (Aldrich), and V_2O_5 (Alfa Aesar). The La_2O_3 and SrCO_3 were heated to 1273 K for 6 hours prior to mixing to remove any adsorbed moisture.⁴ The La_2O_3 , SrCO_3 , and V_2O_5 and YSZ grinding media (5 mm diameter spherical particle, 5 mol% Y_2O_3 , 95 mol% ZrO_2) were then combined in a polyethylene bottle in isopropanol and ball milled for 12 hours. Once mixed the solution was separated from the grinding media placed in a drying oven to remove the solvent. Once dried this solid powder may be either sintered directly or formed into a pellet using a laboratory press and a mold (pellet pressing was required for bulk conductivity tests). The powder or pellet was then calcined at 973 K in air for 10 hours. Samples were then reduced in H_2 to form the desired reduced Sr doped LaVO_3 structure prior to testing.

2.3 Electrochemical Testing

2.3.1 Cell Testing Preparation

After a total cell is constructed, further steps were taken to prepare the cell for performance testing. First, silver wires were attached to the electrodes with silver paste. Silver paste remains porous allowing for the feed gas to reach the electrode surface during testing. Also, silver paste is an effective current collector in H_2 at high operating temperatures but not an effective oxidation catalyst and therefore will not affect the results of catalytic tests.^{1,5}

Once the silver wires were attached, the cell was bonded to an alumina tube with Aremco Ceramabond 552-VFG, shown in Figure 2.3. The ceramabond, once cured, partitions the anode from the cathode and prevents the mixing of air and fuel. The cathode was simply exposed to air during testing, while the anode was exposed to the desired fuel gas (H_2 , CH_4 , etc).

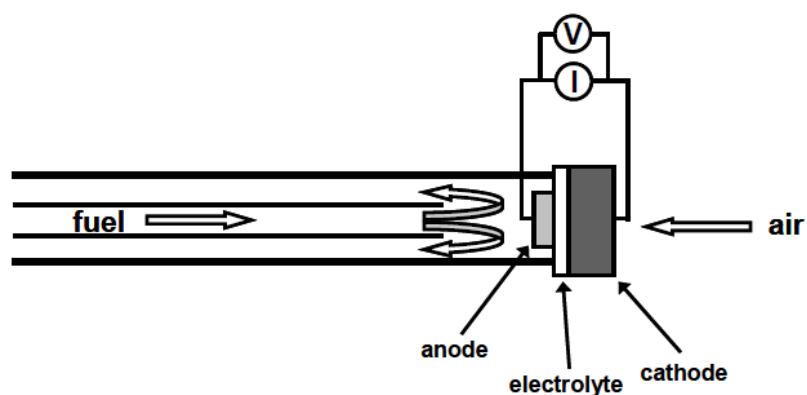


Figure 2.3 Schematic of fuel cell bonded to alumina tube.¹

2.3.2 Flow System

A flow system was utilized to deliver fuel to the testing device, shown in Figure 2.4. Compressed cylinders stored the available fuels; Air, CH₄, H₂, and He. The fuel flow rate was controlled with a flow meter. A fuel flow rate of 40mL/min was used for all tests. Prior to reaching the fuel cell, the incoming fuel was passed through a water bubbler to humidify the incoming fuel. Humidification is required to establish a defined open circuit voltage. The exhaust, which consists of excess fuel and products from the anode side, was vented to a fume hood. The silver wires attached to the cell were coupled with leads connected to a potentiostat.

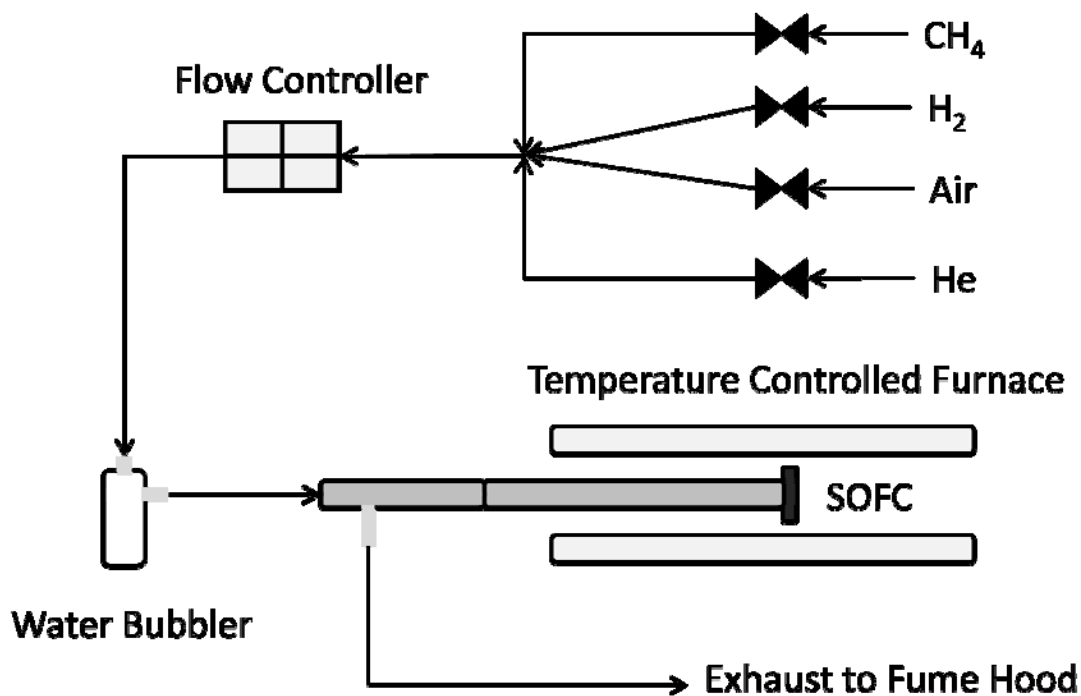


Figure 2.4 Schematic of Flow Control System.

2.3.3 V-i Curve

Two of the most important measurements of fuel cell performance are the voltage-current density, V-i, polarization curve and the power density-current density, P-i, curve. The V-i and P-i curves are often presented together on one plot, as shown in Figure 2.5. In Figure 2.5, the V-i curve is the white squares and the black squares correspond to power density. The slope of the V-i curve is equivalent to the total resistance of the cell according to the equation $V=i \cdot R$. P-i data was generated from the V-i data through the equation $P = V \cdot i$. Power density is displayed in order to compare maximum power density.

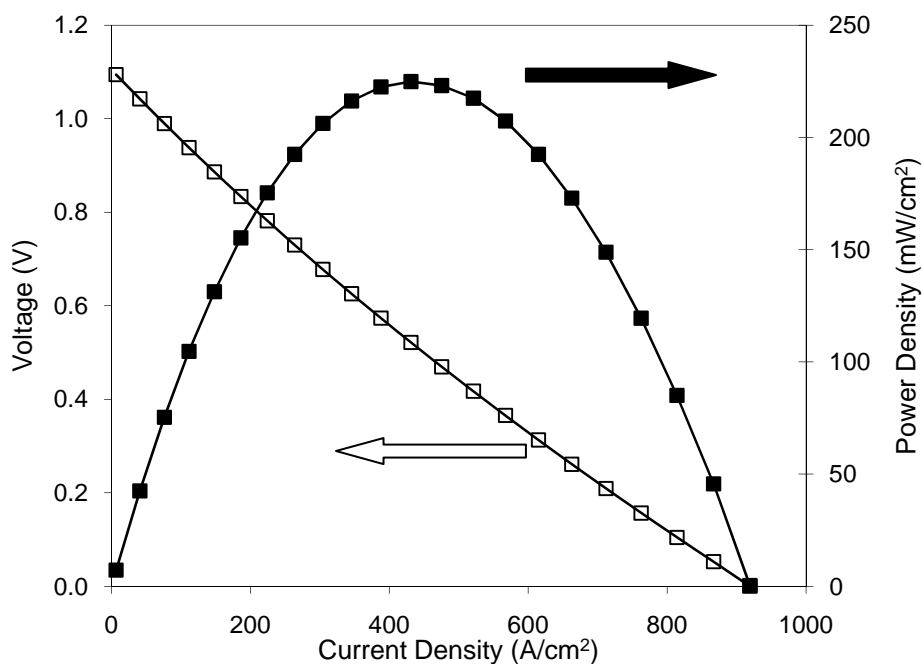


Figure 2.5 V-i and P-i curves for infiltrated LSCM-YSZ anodes with Pd catalyst at 923K in Humidified H₂ (~3% H₂O).

All voltage-current density data was collected with a *Gamry Instruments Series G 750 potentiostat/galvanostat/ZRA*. During testing, the voltage was ramped from open circuit voltage (OCV), which occurs at 0 current density, to 0 V at a rate of 0.05V/s and a constant frequency of 1 Hz. A four point probe experimental set up was utilized to account for the resistance within the lead wires.

2.3.4 Electrochemical Impedance Spectroscopy

The V-i and P-i curves are useful for determining the overall resistance and the maximum power density of the fuel cell. However, V-i and P-i curves are not able to effectively differentiate between the ohmic and non-ohmic losses. Ohmic losses are frequency independent and are attributed to conduction losses within the cell, while non-ohmic losses are frequency dependent and are attributed to kinetic losses. Therefore, changes in ohmic losses are attributed to changes in the cells conductivity, while changes in non-ohmic losses can be attributed to changes in the effectiveness of the catalyst.

Electrochemical impedance spectroscopy (EIS) was utilized in order to quantify and differentiate the ohmic and non-ohmic losses. EIS works by inducing a sinusoidal potential perturbation through the fuel cell over a large range of frequencies, resulting in a sinusoidal current response which is recorded by the *Gamry Instruments G 750*, as shown in Figure 2.6. The resulting phase shift that occurs between the induced sinusoidal potential curve and the resulting current response is used to determine impedance, Z . By plotting the real component of the impedance versus the negative imaginary impedance value, Figure 2.7 is generated. In Figure 2.7, the ohmic resistance is equal to the distance

between the origin and first real impedance value while the non-ohmic resistance is equal to the length of the figure. The total resistance is equal to the sum of the resistances and should be equivalent to the slope of the original V-i plot. EIS data is generally presented with a corresponding V-i plot

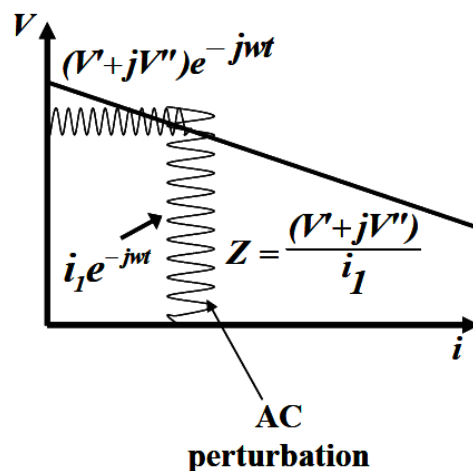


Figure 2.6 Electrical impedance spectroscopy technique.¹

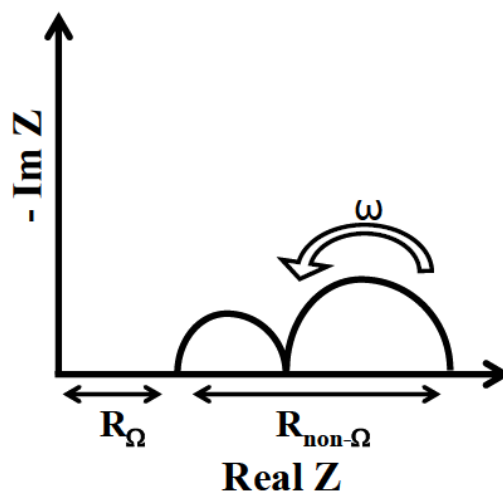


Figure 2.7 Real versus Imaginary impedance showing ohmic and non-ohmic losses.¹

2.3.5 Conductivity Testing

Although changes in the ohmic losses are related to changes in conductivity, there are other factors such as thickness and operating temperature which can affect a cells ohmic losses. Conductivity of a particular material can be directly tested using either infiltrated porous slabs or a pellet made from bulk powders. Regardless of the sample type, the same procedure is used for both types of conductivity tests.

Conductivity is determined by Equation 1.1 below. The resistance is determined by measuring multiple voltage-current pairs using the *Gamry Instruments G 750* and averaging the resistance ($V=iR$). Knowing the resistance and the sample dimensions, one can calculate the conductivity of a sample. The pellets used for conductivity testing were shaved into long rectangular blocks to minimize the cross-sectional area of the sample while maximizing the length between the silver testing wires as shown in Figure 2.8. A rectangular block geometry was chosen because samples often had a high resistance at low temperatures. After wires were attached to the sample, samples were loaded into a custom ceramic tube which was placed into the testing furnace and filled with H_2 during testing.

$$\sigma = \frac{l}{RA} \quad (1.1)$$

where:

- σ is the conductivity in S/cm
- l is the thickness between the wires in cm
- A is the cross-sectional area of the sample in cm^2
- R is the resistance in ohms

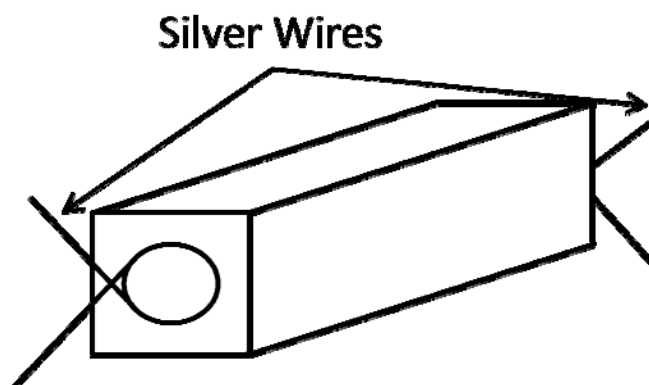


Figure 2.8 Diagram of a Slab Ready for Conductivity Testing.

2.4 Phase and Microstructure Measuring Techniques

2.4.1 Powder X-ray Diffraction

In order to determine the phases present in a sample, powder samples were tested utilizing powder X-Ray Diffraction (XRD). XRD works by directing X-rays at a powder sample over a wide range of angles. When X-rays are directed at atoms the electrons around the atoms oscillate with the same frequency as the incoming X-rays. These oscillations cause destructive interference in almost all directions around the sample. If, however, the atoms within the sample are arranged in a regular pattern (a defining feature of crystalline solids) then in some directions constructive interference will occur and well defined x-rays will leave the sample. The angle at which these x-rays leave the sample may be described by Braggs Law (equation 1.2).⁶

$$n\gamma = 2d \sin 2\theta \quad (1.2)$$

where:

- n is the order of reflection (generally 1)
- γ is the wavelength
- d is the inter-planar spacing
- 2θ is the angle of the x-rays

Databases with the inter-planar spacing of known substances are converted to 2-theta values which are then compared to the 2-theta values measured from a sample.⁷ By comparing all the peaks generated from the XRD to the inter-planar spacing one may

determine then number of phases or crystal structures present in a sample. For this research a *PANalytical X'pert PRO MPD Diffractometer* was used with a $\frac{1}{4}$ " slit size to collect x-ray data in the range of $20 < 2\theta < 80$ degrees using Cu K α radiation.

2.4.2 Thermal Gravimetric Analysis

Thermal Gravimetric Analysis (TGA) was utilized to test the redox stability of samples. TGA measures a change in mass in relation to a change in temperature in a controlled gas environment. This was completed with a *SDT Q600* from TA Instruments. The purge gas was flowed through the TGA at a constant volumetric flow rate of 100ml/min and all samples were tested in ceramic pans. By performing TGA with different purge gasses (Air or 5% H₂/95% Ar) samples can be subjected to reducing and oxidizing environments. By plotting the change in weight percent in relation to change in temperature one may then determine the temperature of oxidation or reduction. If a sample lost the same percent of weight in the reducing environment as it gained in the oxidizing environment then the sample was considered to have reversibly reduced and oxidized, and therefore be redox stable.

2.4.3 BET Isotherm

A BET isotherm test measures the surface area of a sample by submerging a glass tube housing the sample in a liquid nitrogen bath. A *Tristar II 3020 Surface Area Analyzer* (Micromeritics) using Kr adsorption at 78K was utilized to conduct a BET isotherm test to examine the surface area of a porous slab or bulk powder sample. The

Tristar then pumps a precise volume of krypton into the glass tube and measures the change in pressure. At such a low temperature only a single layer of Kr molecules will adsorb onto the surface of a sample and so by measuring the change in pressure within the test tube, the number of krypton atoms adsorbed onto the surface of the sample can be determined and knowing the radius of a krypton atom, the surface area of the sample is also determined.

2.5 References

1. Gross, M.D. PhD Dissertation, University of Pennsylvania; 2007.
2. Simner, S.P.; Bonnett, J.F.; Canfield, K.D.; Mienhardt, V.L.; Sprenkle, V.L.; Stevenson, J.W. Optimized Lanthanum Ferrite-Based Cathodes for Anode Supported SOFCs. *Electrochemical and Solid-State Letters.*; **2002**, A173-175.
3. Rossmeisl, J.; Bessler, W.G. Trends in Catalytic Activity for SOFC Anode Materials. *Solid State Ionics.* **2008**, 178, 1694-1700.
4. Cheng, Z.; Zha, S.; Aguilar, L.; Liu, M. Chemical, Electrical, and Thermal Properties of Strontium Doped Lanthanum Vanadate. *Solid State Ionics.* **2005**, 176, 1921-1928.
5. Channa, K.; De Silvaa, R.; Kasemana, B. J.; Bayless, D. J. Silver (Ag) as Anode and Cathode Current Collectors in High Temperature Planar Solid Oxide Fuel Cells. *International Journal of Hydrogen Energ.* **2011**, 36, 779-786.
6. Scintag Inc Customer Manual. Basics of X-ray Diffraction. Chapter 7, 1999.
7. Hull, A. W.; A New Method of Chemical Analysis. *From the Research Laboratory of General Electric.*1919.

Chapter 3 Effect of Microstructure on Anode Catalytic Performance for Co-Sintered and Infiltrated LSCM

3.1 Introduction

One potential replacement for nickel is $\text{La}_{0.8}\text{Sr}_{0.2}\text{Cr}_{0.5}\text{Mn}_{0.5}\text{O}_3$ (LSCM). LSCM has been shown to have acceptably high electron conductivity, stable operation with methane, and good redox stability.¹ However, LSCM lacks catalytic activity for fuel oxidation. One approach to increasing catalytic activity is to dope the LSCM with well known oxidation catalysts such as Pd or CeO_2 .^{2, 3} Previous research has explored the effects of such catalysts, however the literature presents inconsistent conclusions concerning the effectiveness of Pd in LSCM anodes.^{4, 5}

3.1.1 Effectiveness of Pd in Co-sintered and Infiltrated Cells

The motivation for this research comes from two conflicting conclusions concerning the effectiveness of Pd with LSCM conductive ceramics in SOFC anodes. One research group utilized co-sintered LSCM/YSZ anodes infiltrated with Pd catalyst and concluded that there was “an insignificant effect of Pd nano-particles on the electro-catalytic activity of the LSCM/YSZ” (Figure 3.1a).⁴ This result is unexpected because Pd is documented as an excellent oxidation catalyst.³ At the same time, another group utilized infiltrated LSCM/YSZ anodes with infiltrated Pd and concluded “outstanding anode performance can be achieved using electrodes formed by infiltration of LSCM and catalytically active transition metals into porous YSZ” (Figure 3.1b).⁵

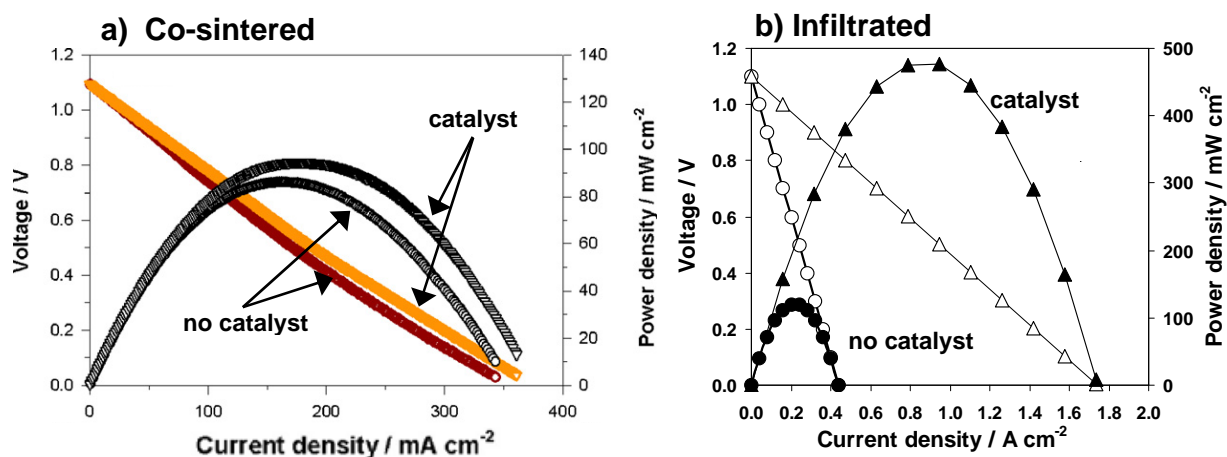


Figure 3.1 Cell performance curves for LSCM-YSZ anodes without Pd catalyst (circles) and with infiltrated Pd catalyst (triangles) in humidified H₂ (3% H₂O). a) LSCM-YSZ co-sintered at 1473 K in air⁴ b) YSZ sintered at 1823 K in air followed by infiltration of LSCM and calcination at 1473 K in air.⁵

Looking at Figure 3.1 one can see that there is an obvious difference in improved performance between cells with Pd catalyst and without Pd catalyst. The only difference between the fuel cells was that one anode was constructed with a porous co-sintered LSCM-YSZ structure while the other was constructed with a porous YSZ structure into which LSCM was infiltrated. We hypothesized that the performance difference between these two studies can be attributed to microstructure differences at the activation region of the anode created by the respective methods of construction.

3.2 The Effect of Fabrication Method on Microstructure

Traditionally, ceramic anodes are constructed by co-sintering. Co-sintering involves sintering the conductive ceramic, in our case LSCM, with YSZ at high temperatures. This method results in a random mixture of the YSZ and LSCM. Once the porous LSCM-YSZ structure is formed, Pd catalyst is then infiltrated into the structure. In traditional anodes using Ni, the points where the Ni, YSZ and fuel meet is known as the three phase boundary (TPB) because three components must meet (the fuel coming from a porous channel, the YSZ, and the electron conductor), shown in Figure 3.2a. When the electron conductor and catalyst are separated such as in a co-sintered LSCM-YSZ anode, the active site requires four materials to be present to form an active site (the LSCM, the catalyst, the fuel, and the YSZ) shown in Figure 3.2b. Increasing from a three to four phase boundary decreases the probability of an activation site occurring.

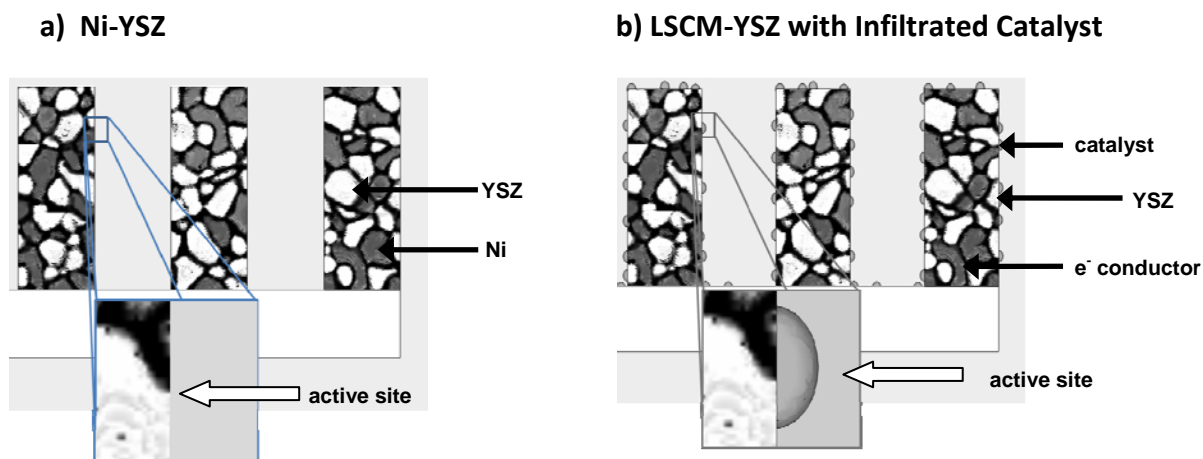


Figure 3.2 Schematic of a) a Ni-YSZ anode and b) a YSZ anode with separate e⁻ ceramic conductor and catalyst.

Knowing the microstructure of a four phase boundary within a co-sintered anode (Figure 3.3a), it is now necessary to understand how infiltration changes the active region. Infiltration creates a layered structure where the LSCM coats the YSZ surface. The Pd catalyst is then infiltrated after the LSCM is infiltrated. With the LSCM and Pd infiltrated into the porous YSZ scaffold, it is theorized that the microstructure would appear more like Figure 3.3b changing the probability of activation sites forming. We hypothesize that the co-sintered and infiltrated microstructure may differ greatly and have a significant impact on the catalyst effectiveness within the anode, thereby explaining the poor performance of the Pd catalyst with the co-sintered anodes and excellent performance of the infiltrated cells.

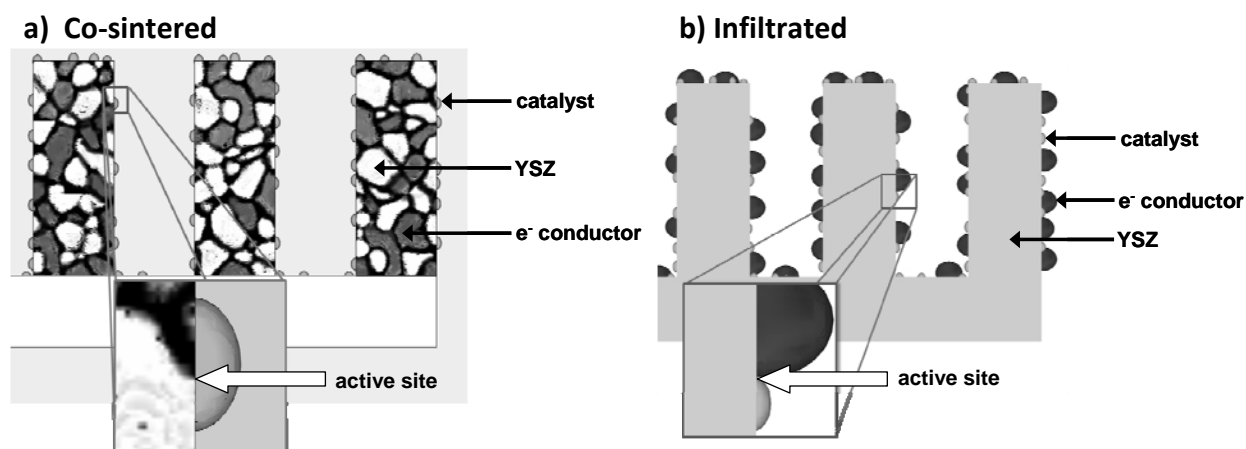


Figure 3.3 Schematic of a) a co-sintered ceramic conductor/YSZ anode with an infiltrated catalyst and b) a sintered YSZ anode with infiltrated ceramic conductor and catalyst.

In order to test our hypothesis that the microstructure is the fundamental cause of the reported difference between the co-sintered and infiltrated cells, an experiment was

designed which would allow a direct performance comparison of infiltrated and co-sintered anodes.

3.3 Experimental

In order to test the effect of anode microstructure on performance, three types of cells were created with identical compositions, shown in Table 3.1. First ‘A’ cells were made in the same fashion as the co-sintered cells utilizing a co-sintered LSCM and YSZ paint. ‘B’ cells were infiltrated cells with a porous YSZ scaffold and infiltrated LSCM anode. Both ‘A’ and ‘B’ type cells were made with and without Pd catalyst and it was expected that both cell’s performance should closely match the previously published studies. In order to make a direct comparison, both the ‘A’ and ‘B’ cells were constructed with the same vol% of LSCM, YSZ, and porosity. All anodes in this study were created to be 40 vol% porosity, 35 vol% YSZ, and 25 vol% LSCM. Cathodes were prepared with LSF to a final loading of 30 wt% of the cathode. In this study the cathode was 230 μ m thick, the electrolyte was 50 μ m thick and the anode was 60 μ m thick. The manufacturing methods used to construct these fuel cells are described in section 2.1.

Table 3.1 Anode Configurations for Fuel Cell Testing.

Cell	Fabrication Method	Catalyst
A	LSCM Co-sintered	none/Pd
B	LSCM Infiltrated	none/Pd

All fuel cells tests included electrochemical impedance spectroscopy and V-i measurements. Tests were conducted between 923-1173 K in both humidified hydrogen

and methane (humidified = 3% H₂O). It was expected that performance would improve with increased temperature. As previously stated, the compositions of the anodes, the electrolyte, and the cathode were identical, so that differences in performance can be directly attributed to the anode microstructure. Performance data from 'A' and 'B' cells match the results from the previously reported co-sintered and infiltrated studies.

3.4 Results

Figure 3.4 shows V-i and P-i curves of ‘A’ and ‘B’ type cells taken at 973 K. The data presented in Figure 3.4 is representative of all temperatures tested (923-1173 K). The ‘B’ infiltrated cells performed as expected. Without catalyst, the infiltrated LSCM-YSZ cell had a maximum power density of 25mW/cm² and with the addition of a catalyst the maximum power density improved to 350mW/cm². This is very similar to the data previously reported for infiltrated LSCM-YSZ cells (Figure 3.1b).

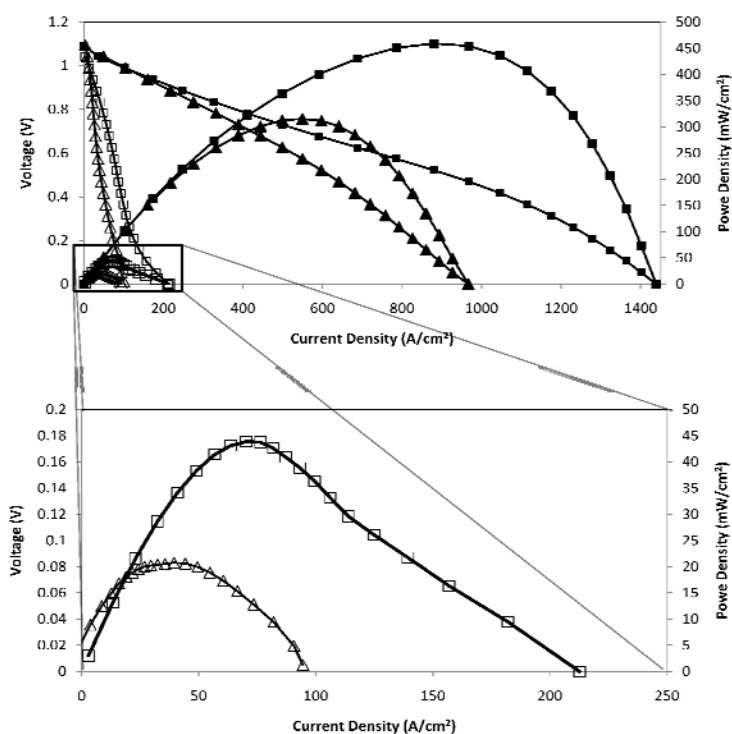


Figure 3.4 Comparing cell performance of ‘A’ LSCM-YSZ co-sintered anode with and without Pd catalyst (black squares and white squares respectively) and ‘B’ LSCM-YSZ Infiltrated anode with and without Pd catalyst (black triangles and white triangles respectively) at 973K in Humidified H₂.

Figure 3.4 also shows some unexpected results. The ‘A’ cells do not match the previously reported co-sintered LSCM-YSZ cells (Figure 3.1a). In the previous study, co-sintered cells without Pd had a power density of $90\text{mW}/\text{cm}^2$ and cells with Pd had a power density of $100\text{mW}/\text{cm}^2$. However, our co-sintered cells without Pd exhibited a maximum power density of about $45\text{mW}/\text{cm}^2$ and with catalyst, a maximum power density of $450\text{mW}/\text{cm}^2$ with catalyst, an increase of a factor of 10. Immediately we see that our results are in conflict with the previously reported results.

Figure 3.4 also shows that with identical compositions, the ‘A’ co-sintered cell had a higher maximum power density than the ‘B’ infiltrated cells. This too is unexpected based upon our hypothesized microstructure at the activation site. It was believed that the infiltrated cells would have a higher density of active sites and therefore would exhibit a higher maximum power density than the co-sintered cells. It is clear that a dramatic improvement in anode performance was observed in both cases after the addition of Pd.

There are several possible reasons for the discrepancy between our co-sintered LSCM data and the previously published co-sintered work. The previous study’s cells may not have been fabricated properly resulting in an ineffective anode. Another possible explanation is that some other part of the cell (electrolyte or cathode) was performing poorly enough to mask the effect of the catalyst.

Looking back at the data we see that my co-sintered cell had a total resistance of $0.65\ \Omega$, while the previous study had an ohmic resistance of $2\ \Omega$, almost 3 times greater

than my co-sintered cells total resistance. This high ohmic resistance means that the any benefit of the Pd catalyst was masked by the poor conductivity of the cell.

3.5 Conclusions

From this study we may conclude that it is possible to significantly improve the anode performance of co-sintered LSCM-YSZ anodes with the addition of a Pd catalyst. In fact, the performance is comparable for infiltrated and co-sintered LSCM-YSZ anodes infiltrated with a Pd catalyst. Based on our results, the lack of performance enhancement with the addition of Pd that was reported in previous studies was not a result of anode microstructure but instead was caused by some other part of the cell masking the effect of the Pd catalyst with high conductive losses.

3.6 References

1. Tao, S.; Irvine, J.T.S. Synthesis and Characterization of $(\text{La}_{0.75}\text{Sr}_{0.25}\text{Cr}_{0.5}\text{Mn}_{0.5}\text{O}_{3-\delta})$, a Redox-Stable, Efficient Perovskite Anode for SOFCs. *Journal of Electrochemical Society*. **2004**, 151, 252-259.
2. Bidrawn, F.; Kim, G.; Corre, G.; Irvine, J. T. S.; Vohs, J. M.; Gorte, R. J. Efficient Reduction of CO_2 in a Solid Oxide Electrolyzer. *Electrochemical and Solid-State Letters*. **2008**, B167-B170.
3. Rossmeisl, J.; Bessler, W.G. Trends in Catalytic Activity for SOFC Anode Materials. *Solid State Ionics*. **2008**, 178, 1694-1700.
4. Jiang, S.P.; Ye, Y.; He, T.; Ho, S.B. Nanostructured Palladium- $\text{La}_{0.75}\text{Sr}_{0.25}\text{Cr}_{0.5}\text{Mn}_{0.5}\text{O}_3/\text{Y}_2\text{O}_3\text{-ZrO}_2$ Composite Anodes for Direct Methane and Ethanol Solid Oxide Fuel Cells. *Journal of Power Sources*. **2008**, 185, 179-182.
5. Kim, G.; Corre, G.; Irvine, J. T. S.; Vohs, J. M.; Gorte, R. J.; Engineering Composite Oxide SOFC Anodes for Efficient Oxidation of Methane. *Electrochem Solid-State Lett*. **2008**, B16-B19.

Chapter 4 Investigation of LSV for use as a Potential Electron Conductor in SOFC Anodes

4.1 Introduction

Strontium doped lanthanum vanadates (LSV) are attractive potential candidates for SOFC anodes because of their extremely high conductivity. However, there are few reports on the performance of LSV in fuel cell applications. The goal of this project was to complete fundamental material characterization analysis on LSV and fuel cell performance tests in order to assess the effectiveness of LSV in SOFC anodes.

4.1.1 Motivation

Early investigations into strontium doped lanthanum vanadates ($\text{La}_{1-x}\text{Sr}_x\text{VO}_3$) for use in fuel cells came from two literature reports. One found that LSV exhibited good conductivity in the presence of H_2S .¹ The second study noted that lanthanum vanadates were chemically compatible with YSZ and achieved good conductivity in both pure H_2 and CH_4 , but noted that LSV was not a good oxidation catalyst.² The data published from these sources showed that LSV had the potential to be a good electron conductor in SOFC anodes under a variety of fuels. The fact that LSV was reported as a poor oxidation catalyst was not worrisome because through infiltration an additional oxidation catalyst, such as Pd, could be added to the anode.

4.2 Experimental

In our investigation of LSV, we defined an optimal LSV composition to be one which had the highest electronic conductivity while maintaining a single phase after undergoing a cycle of oxidation and reduction redox conditions. It has already been suggested that increasing the doping of Sr within LSV would result in an increased conductivity. However, we believed that at some point the Sr doping concentration would reach a critical level where two separate oxide structures form, SrVO₃ and LaVO₃, as opposed to the desired Sr doped LaVO₃. Therefore bulk powders of LSV were made with varying compositions and XRD was utilized to identify those compositions that are single phase.

Powders were made according to the procedure described in section 2.2.6. Before testing with XRD, powders were reduced at a high temperature, 1673 K, in H₂ for 10 hours in order to determine if a reduced single phase was possible. After this initial reduction, the powder samples were oxidized in air at 973 K for 10 hr and then reduced again in H₂ at 973K for 10hrs, completing a full redox cycle. XRD tests were conducted after the initial high temperature reduction and again after the redox cycle.

TGA was also performed on each powder sample. TGA was used to confirm whether or not the powders were fully and reversibly reducing, which could be determined by examining the weight change in a sample. Samples were reduced in 5% H₂/95% Ar and oxidized in air with a flow rate of 100 ml/min. All samples were heated at a constant rate of 2 K/min until they reached 973 K and then held at 973 K for 10 hours.

Bulk powders for conductivity tests were constructed as described previously in section 2.26. The 1 g pellets were heated to 1673 K for 10 hours to ensure the entire pellet completely reduced. Bulk conductivity tests were completed at temperatures ranging from 923 – 1123 K with readings being taken at 50 K increments in humidified H₂.

Porous slabs for conductivity testing were created by the methods described previously in section 2.2.5. The slabs were infiltrated with the previously described LSV solution to a final loading of 15 vol%. Porous Slab conductivity tests were conducted at temperatures ranging from 923 – 1123 K with measurements taken every 50 K in humidified H₂.

Fuel cells were prepared according to the procedure described previously in sections 2.2.1 – 2.2.4. Fuel cells in this project had an 80 μm thick electrolyte and 40 μm thick 65% porous electrodes. LSV was infiltrated into porous YSZ to a final loading of 10 vol%. CeO₂ (1 M Ce(NO₃)₃ Alfa Aesar, 99.5%) and Pd (0.45M Tetraammine palladium (II) nitrate solution, Alfa Aesar 99.9%) were added as catalysts to a final loading of 2.8 vol% and 0.5 vol% respectively. For comparison purposes, a third cell was prepared with 20 vol% LSCM and a Pd/ceria catalyst loaded to a final loading of 2.4 vol% and 0.42 vol%, respectively, utilizing the previously described LSCM infiltration methods.

4.3 Results

4.3.1 Powder X-ray Diffraction of various LSV compositions

Figure 4.1 shows the pattern for bulk powders of various compositions of $\text{La}_{1-x}\text{Sr}_x\text{VO}_3$ reduced at 1673 K in H_2 , and after undergoing a redox cycle of both air and hydrogen at 973 K. A standard pattern of LaVO_3 orthorhombic (JCPDS card No. 81-2435) is displayed with each pattern since the single phase crystal structure should match the pattern of LaVO_3 (Figure 16c)). Figure 16b) is the XRD pattern following the initial reduction at 1673 K. Figure 16a) is the XRD pattern following the redox cycle in air and H_2 at 973 K. As the doping level of Sr increased the XRD patterns exhibit a slight shift to a higher 2 theta value. This shift was expected and is attributed to slight distortions created by the size difference between a La and Sr atom (217pm versus 219pm). Figure 16 shows that a single phase structure was observed for compositions with $x = 0.4, 0.3, 0.2, 0.1$ because the initial peak matched the standard. Single phase was also maintained after the redox cycle for these aforementioned compositions because no new peaks appeared in the XRD pattern after the redox cycle. Sr doping levels of $x = 0.5$ and 0.6 did not result in a single phase. The presence of multiple phases was indicated by the appearance of additional peaks. The secondary peaks are positioned close to the identified standard patterns which is expected because SrVO_3 has a very similar structure to LaVO_3 and therefore a similar XRD pattern. Therefore it was concluded that Sr doping levels of greater than $x = 0.5$ do not result in a single phase.

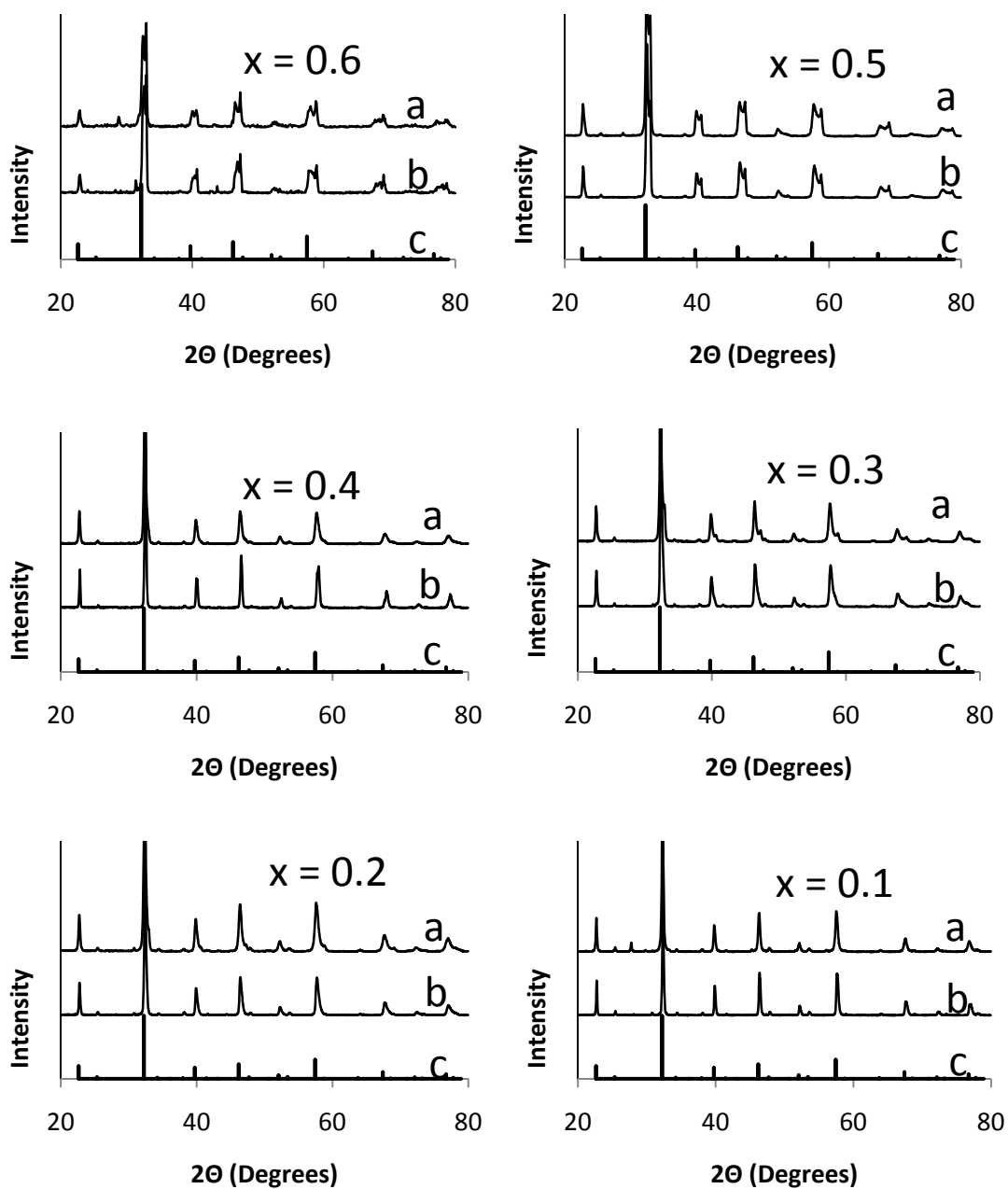


Figure 4.1 XRD patterns of varying compositions of $\text{La}_{1-x}\text{Sr}_x\text{VO}_3$ with a) Post redox cycle, oxidation in air and reduction in H_2 both at 700°C for 10 hours b) Reduced in H_2 at 1400°C for 10 hours c) LaVO_3 standard pattern.

4.3.2 Thermal Gravimetric Analysis

XRD data confirmed that it was possible to achieve a single phase redox stable ceramic. However, it is not feasible to initially reduce LSV to 1673 K in a fuel cell. Therefore, TGA was employed to verify the previous data and to determine the temperature at which LSV samples reduced. Figure 4.2 shows TGA data of $\text{La}_{0.7}\text{Sr}_{0.3}\text{VO}_{2.85}$ oxidized in air to $\text{La}_{0.7}\text{Sr}_{0.3}\text{VO}_{3.85}$ and then reduced in 5% H_2/Ar . Figure 4.2 also shows that LSV began reducing below 550°C , began oxidizing at approximately 300°C and underwent a reversible weight percent change. This is a very low reduction temperature compared to other metal oxides.

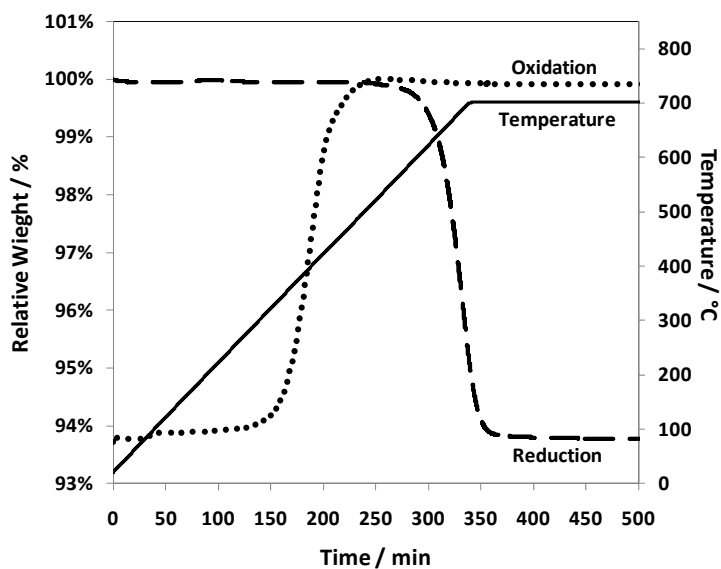


Figure 4.2 TGA curves for the reduction of $\text{La}_{0.7}\text{Sr}_{0.3}\text{VO}_{3.85}$ in 4% H_2/Ar and oxidation of $\text{La}_{0.7}\text{Sr}_{0.3}\text{VO}_{2.85}$.

4.3.3 Analyzing the Anode Microstructure with SEM and BET Isotherm

In order to gain qualitative data on the LSV microstructure within a porous composite, SEM micrographs were taken of LSV-YSZ composites calcined at 973K and 1373K before and after reduction at 973K, shown in Figure 4.3. Figure 4.3a shows the YSZ scaffold before adding the LSV. After adding LSV and sintering at 973 K the porous YSZ scaffold appears to be coated with a uniform layer of LSV, Figure 4.3b. After reduction at 973K the uniform layer of YSZ appears to have small fractures, Figure 4.3c. Figure 4.3d shows that calcination at 1373K causes the LSV film to no longer be a uniform coating but a jagged film resting on the YSZ surface. Again, reduction causes large cracks to appear within the LSV structure, Figure 4.3e.

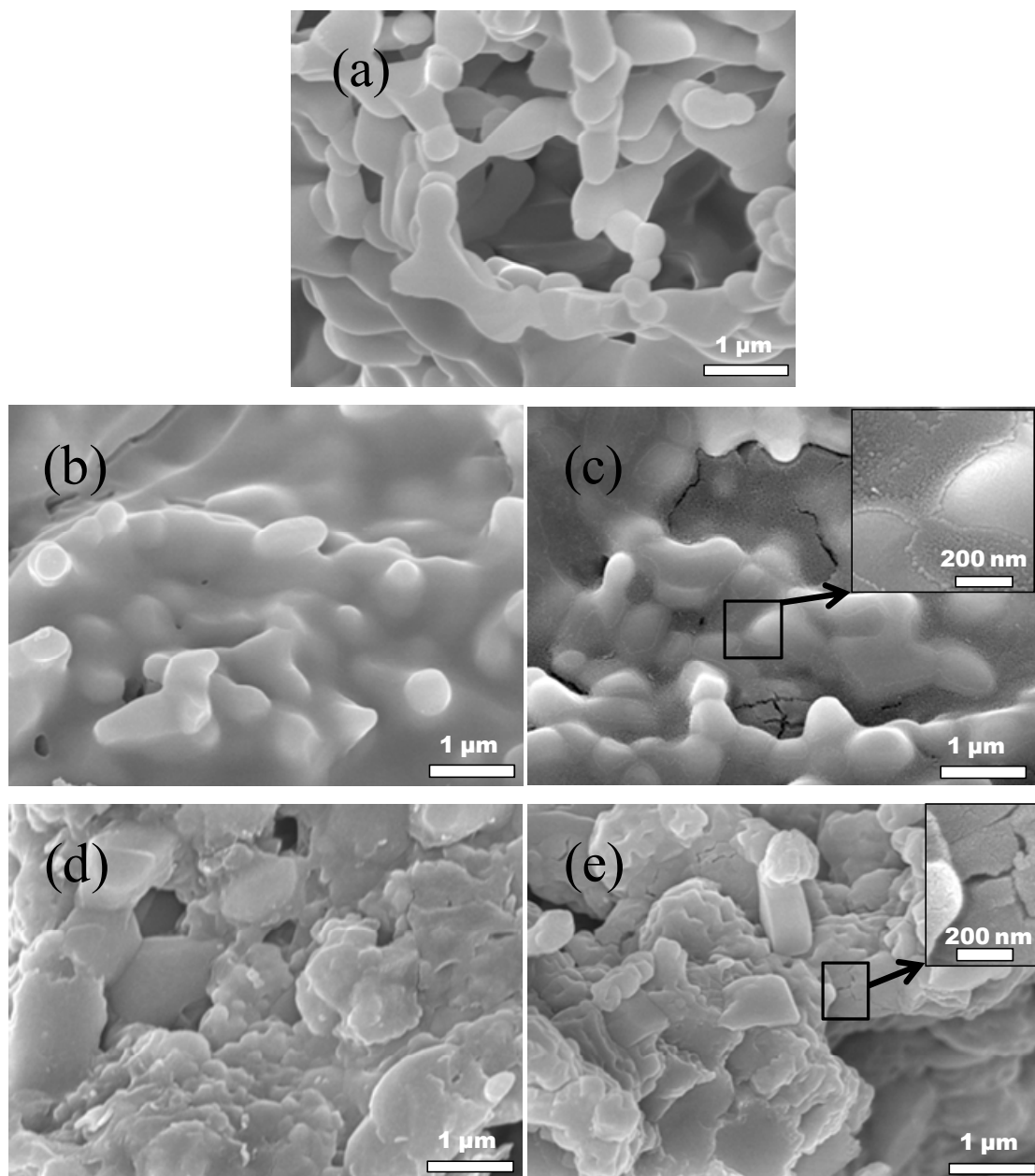


Figure 4.3 SEM images of (a) the initial YSZ scaffold. The LSV-YSZ composite calcined at 973 K (b) before and (c) after reduction. The LSV-YSZ composite calcined at 1373 K (d) before and (e) after reduction.

The appearance of cracks within the LSV after reduction is similar to what has been reported for LSCM in YSZ.³ It has been argued that these cracks serve to increase the number of active sites by increasing the YSZ-LSV-catalyst-fuel interface. In order to quantify the surface area of these composites, BET isotherm measurements were taken, summarized in Table 4.1. For the LSV-YSZ composites calcined at 973 K the composite had a surface area of 0.13 m²/g which increased to 1.14 m²/g after reduction in H₂ at 973K for 5 hours. The samples which were calcined at 1373 K had a surface area of 0.14 m²/g, which increased to 0.68 m²/g. Based upon these surface area changes it is apparent that sintering at a lower temperature results in a more uniform LSV layer which after reduction creates a microstructure with more surface area, and presumably more activation sites.

Table 4.1 Specific surface areas of LSV-YSZ composites fabricated at 973 K or 1373 K, before and after reduction.

Fabrication temp.(K)	Surface area (m ² /g)	
	Before reduction	After reduction
973	0.13	1.14
1373	0.14	0.68

4.3.4 Conductivity of LSV samples

In order to ensure that LSV is suitably conductive, conductivity data was taken of bulk samples and composites, shown in Figure 4.4. Both the pellet and slab were tested at temperatures ranging from 923 K – 1173 K at 50 K increments. The bulk pellet exhibited

conductivity just above 100 S/cm which is consistent with data from a previous study of LSV by Hui and Petric.⁴ The LSV-YSZ composite exhibited conductivity of 1.5 S/cm which is high enough to serve as an electron conductor in an SOFC.

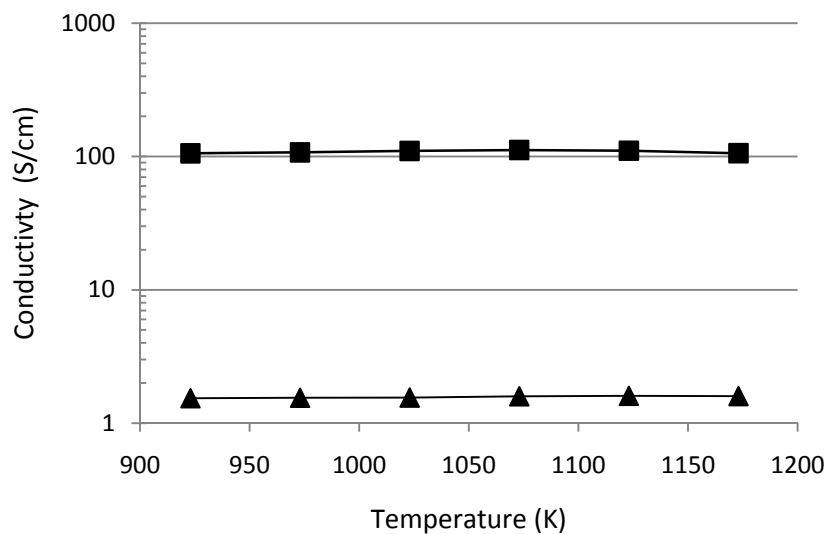


Figure 4.4 Conductivity data for LSV bulk pellet reduced in H₂ at 1773 for 10hrs (squares) and LSV-YSZ composite calcined at 973 k for 10 hours and then reduced during testing (triangles).

4.3.5 Cell Testing

Cell testing was conducted on an LSV cell, with and without catalyst, and an LSCM cell with catalyst for comparison. The results of V-i polarization curves as well as Electrochemical Impedance Spectroscopy (EIS) for all three cells are presented in Figure 4.5. Both LSV cells exhibited the expected open circuit voltage of 1.1 V and the addition of a catalyst increased the maximum power density from 90 mW/cm² to 470 mW/cm².

The addition of catalyst to the LSV cells resulted in an even higher power density than the LSCM-YSZ cell with catalyst, which exhibited a maximum power density of 370 mW/cm².

The EIS data reinforces the results from the V-i polarization curve. Comparing the LSV-YSZ cells, with and without catalyst, Figure 4.5 shows that both cells have the same ohmic resistance, 0.43 Ωcm² but the addition of a catalyst significantly reduces the cells non-ohmic losses by a factor of 10 from 2.5 Ωcm² to 0.2 Ωcm². This significant reduction in activation (non-ohmic) losses indicates that the addition of catalyst is required to obtain good fuel cell performance.

LSV fuel cells were also tested to examine their stability in hydrocarbon fuels. Figure 4.6 shows the V-i polarization curve and EIS plots for LSV fuel cells run in Humidified H₂ (~3% H₂O) and CH₄ at 1073 K. Both cells had the same OCV, 1.1 V, but the power density was significantly higher in the humidified H₂ than the CH₄, 960 mW/cm² and 510 mW/cm² respectively. The impedance data showed that the ohmic resistance of the two cells was identical, but the non-ohmic losses were noticeably higher for the cells in methane. This increase in non-ohmic resistance means that there could be catalytic limitations to breaking the C-H bonds in methane. It is known that CH₄ can form carbon deposits over time when Pd is utilized as a catalyst, however it appears that LSV is not affected by methane since the electrode was stable throughout the testing period.

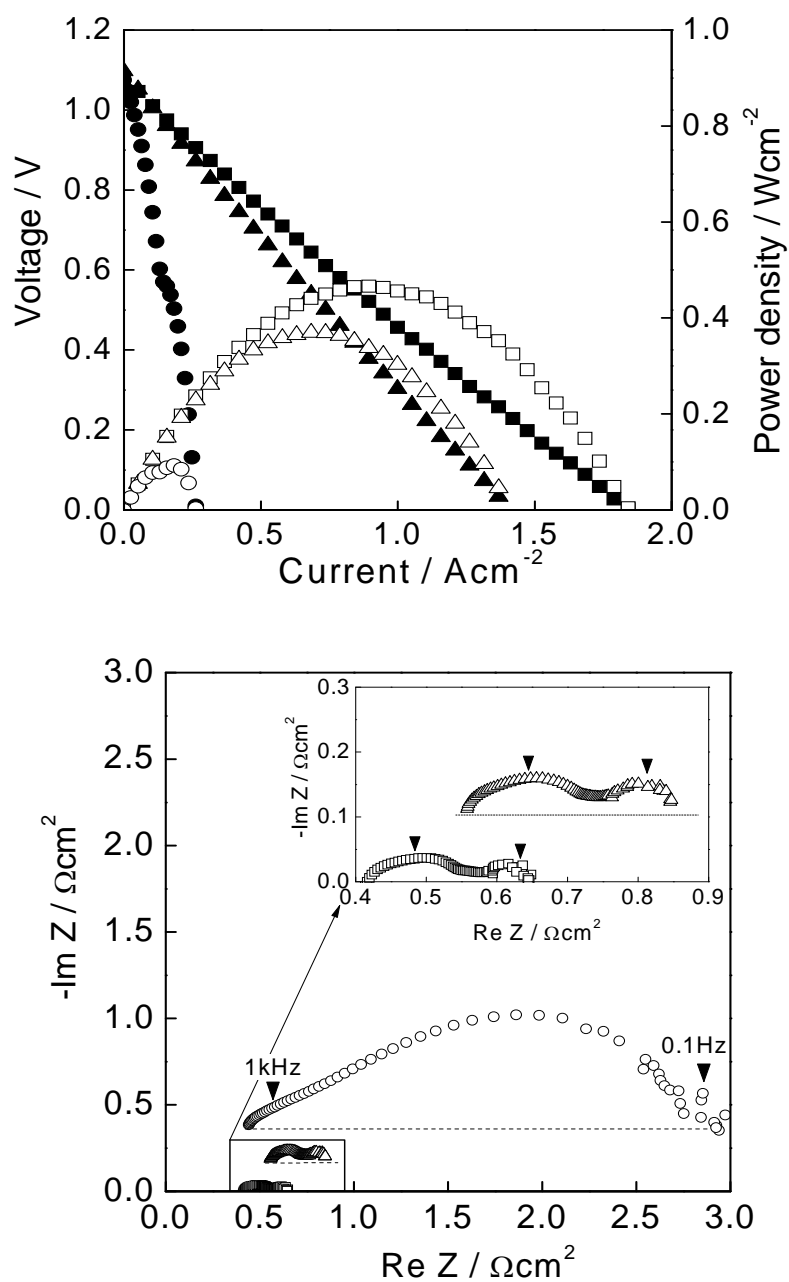


Figure 4.5 V - i polarization curves and impedance spectra of cells at 973 K using LSV-YSZ anode with (■) and without (●) CeO₂ and Pd. Data for the LSCM-YSZ anode with CeO₂ and Pd (▲).⁵

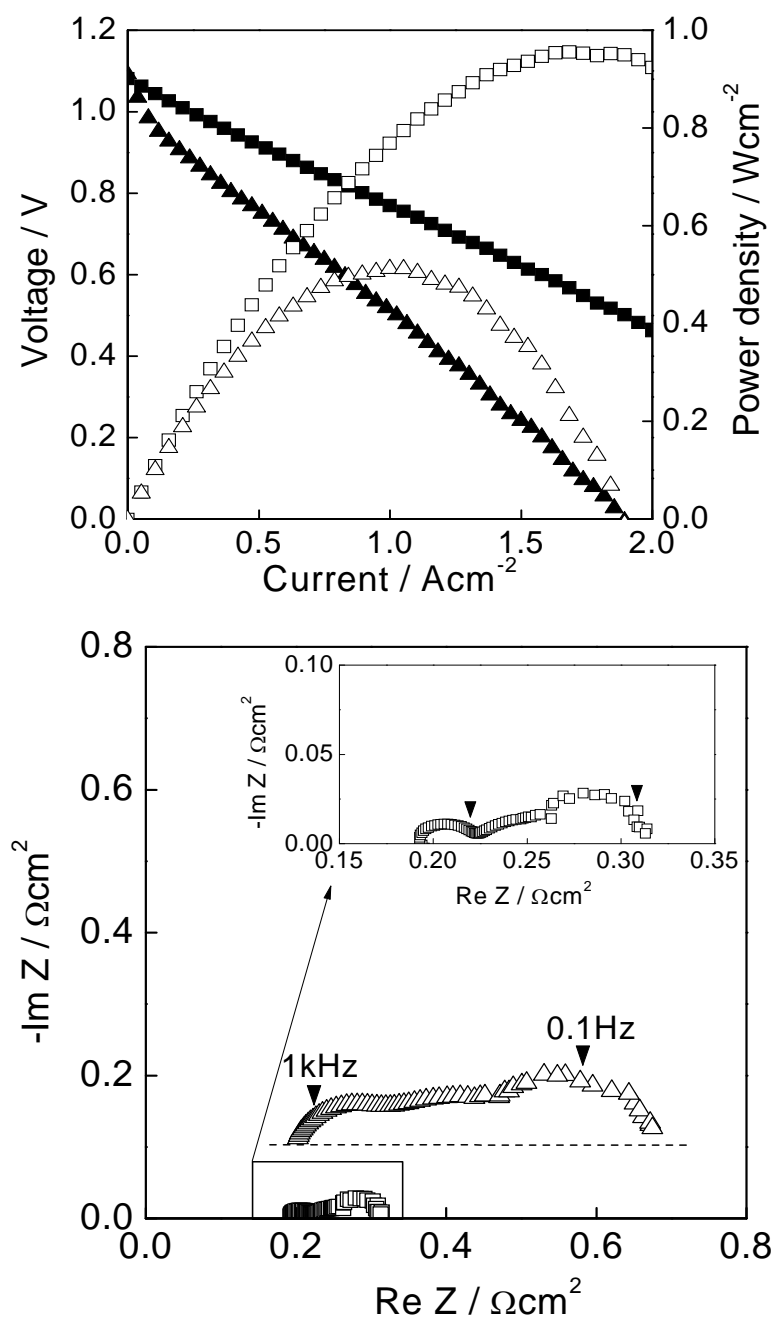


Figure 4.6 $V-i$ polarization curves and impedance spectra of cell having LSV-YSZ anode with CeO_2 and Pd in humidified (3% H_2O) H_2 (■) or CH_4 (▲) at 1073 K.⁵

Industrial scale fuel cells frequently must undergo cycles of oxidation and reduction during startup and shutdown. In order to examine the effects that a high temperature oxygen rich environment would have on a completed cell, a cell was heated to 973 K after the addition of Pd catalyst and is shown in Figure 4.7. It was found that after calcination in air, the cell exhibited a significant loss in performance with power density decreasing from 470 mW/cm² to 280 mW/cm². This change in power density was attributed to an increase in the non-ohmic losses, indicating that there could be a negative interaction between LSV and the catalyst after a complete oxidation cycle.

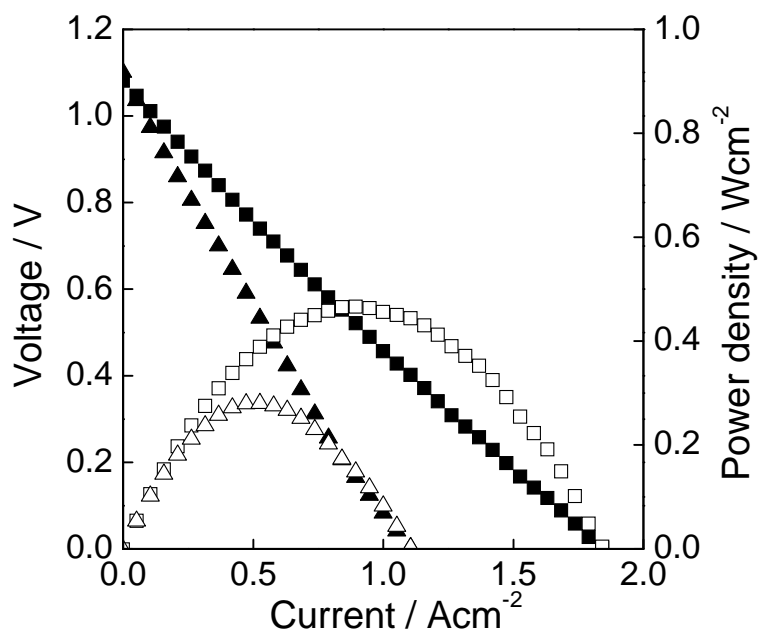


Figure 4.7 V-*i* polarization curves in humidified (3% H₂O) H₂ for cells having LSV-YSZ anodes with Pd/ceria catalysts. Data are shown before (■) and after (▲) heating the composite to 973 K in air.⁵

The aforementioned loss in performance after a redox cycle has not been seen in any other previously tested metal oxide. Since it is known that vanadium is a poison in some catalysis reactions⁶, it seems likely that an interaction between the vanadium and the Pd catalyst may be the cause of this performance decrease. In order to test if vanadium was causing this performance decrease, cells were constructed with varying vanadium stoichiometry $\text{La}_{0.7}\text{Sr}_{0.3}\text{V}_{1+\delta}\text{O}_3$. All cells were calcined at 973 K after the addition of LSV and then calcined again at 973 K after the additions of Pd. Cells were then reduced during testing, the results of which are summarized in Table 4.2. Table 4.2 shows that as the concentration of vanadium decreases within the oxide the maximum power density of the cell increases and the non-ohmic losses within the cell decrease. Table 4.2 indicates that high concentrations of vanadium detrimentally affect the catalysts and improved performance can be had by creating vanadium deficient cells.

Table 4.2 Maximum power densities of the cells at 973 K in humidified H_2 , with anode having 10 vol-% LSV, together with Pd and ceria. In these experiments, the vanadium content of the LSV phase ($\text{La}_{0.7}\text{Sr}_{0.3}\text{V}_{1+\delta}\text{O}_{2.85}$) was varied and the cells were heated to 973 K in air before reduction to study the effect of interactions between the LSV phase and the Pd/ceria catalyst.

Non-stoichiometry of LSV	Power density (mW/cm ²)	Ohmic ASR (Ωcm^2)	Non-ohmic ASR (Ωcm^2)
$\delta = -0.05$	326	0.43	0.49
$\delta = 0$	280	0.45	0.61
$\delta = 0.05$	254	0.45	0.71

4.3.6 Vanadium Deficient Optimization

Discovering that reducing the concentration of vanadium within the metal oxide gave increased performance after calcinations gave rise to two new questions: 1) does varying the concentration of vanadium affect the phase and conductivity of the LSV? and 2) what other catalysts are affected by the concentration of LSV in an oxidation environment? In order to determine the levels of vanadium deficiency that maintain a single phase, XRD was employed. Figure 4.8 shows XRD for various compositions of $\text{La}_{0.7}\text{Sr}_{0.3}\text{V}_x\text{O}_3$. Figure 4.8 is again presented with the LaVO_3 standard plot. It is apparent that $x = 1.0, 0.95,$ and 0.90 all maintain a single phase. At 0.85 an additional peak appears in the 2θ region of 30° . An additional peak indicates that an impurity is being created which was identified to be La_2O_3 . This is logical because as the vanadium concentration is reduced eventually the La will bond directly to the excess oxygen ions. The $x = 0.80$ composition confirms this theory as it clearly displays a larger more defined La_2O_3 impurity peaks. Based upon this data it was concluded that $\text{La}_{0.7}\text{Sr}_{0.3}\text{V}_{0.9}\text{O}_3$ is the maximum of level of vanadium deficiency for LSV before multiple phases are formed.

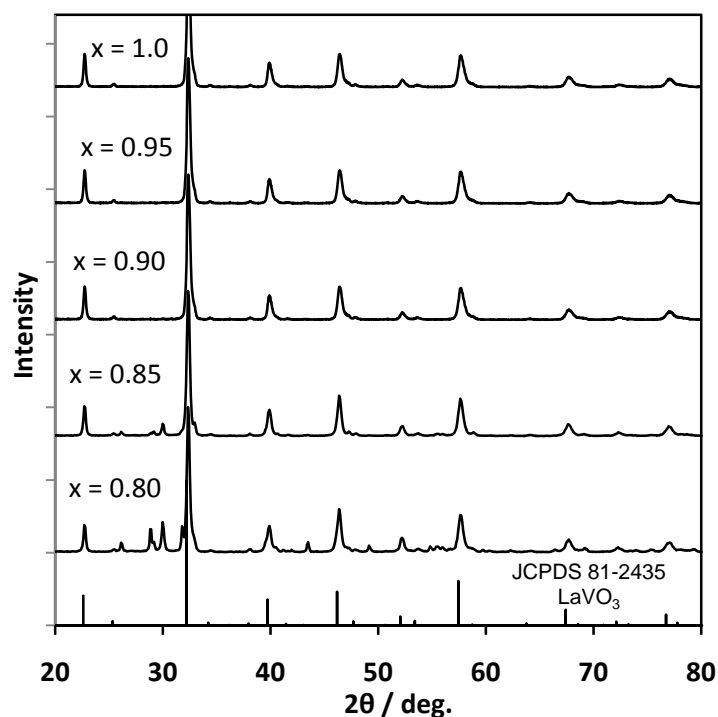


Figure 4.8 XRD plot of varying compositions of $\text{La}_{0.7}\text{Sr}_{0.3}\text{V}_x\text{O}_3$ sintered in Air at 973K for 10hr and reduced in H_2 at 973K for 10hr.

4.3.7 TGA of Vanadium Deficient LSV

After identifying which compositions of vanadium deficient LSV are single phase after reduction, it was necessary to find the temperature at which vanadium deficient LSV reduced. Figure 4.9 is a TGA plot for the reduction of various compositions of $\text{La}_{0.7}\text{Sr}_{0.3}\text{V}_x\text{O}_3$ reduced in 5% $\text{H}_2/95\%$ Ar ramping to 973 K. Figure 4.9 shows that as the LSV becomes more deficient the temperature at which it reduces does not change. Even though the slopes change for each of the three compositions this could be caused by other factors such as the sample size.

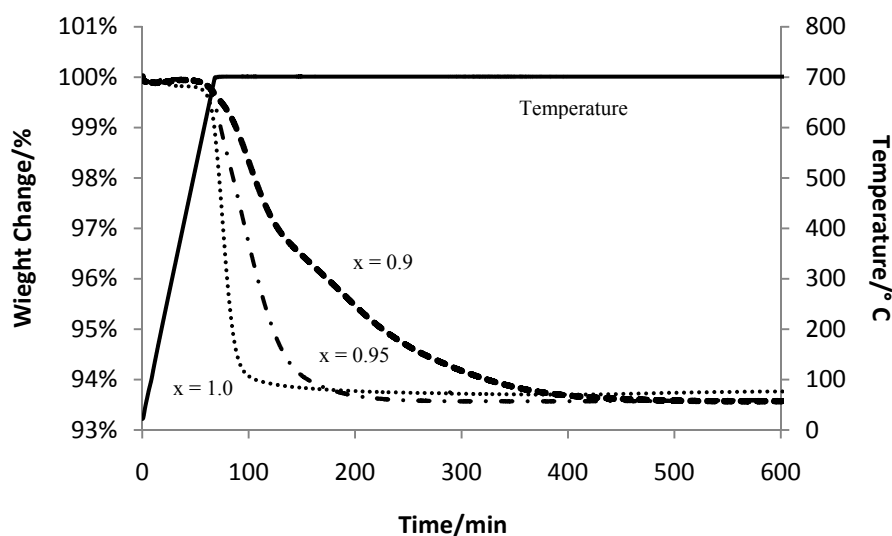


Figure 4.9 TGA curves for the reduction of $\text{La}_{0.7}\text{Sr}_{0.3}\text{V}_x\text{O}_3$ in 5% H_2 /95%Ar Conductivity of Vanadium Deficient LSV.

4.3.8 Conductivity of Vanadium Deficient Slabs

Lastly conductivity data was taken in order to determine if reducing the vanadium composition impacted the conductivity of the anode. Porous slabs were infiltrated with various vanadium deficient compositions to a final loading of 15 vol%. The slabs were heated to 973 K for 10 hours in air and tested in H_2 at temperatures ranging from 973 K to 1173 K shown in Figure 4.10. Figure 4.10 shows that as the concentration of vanadium decreased within the ceramic, the conductivity of the slab also decreased. The decrease in conductivity was only slight from $x = 1.0$ to $x = 0.95$ but a much larger drop in conductivity occurred at the $x = 0.90$ level. This would suggest that the vanadium

vacancies within the ceramic at a vanadium deficiency of $x = 0.90$ inhibit the conduction of electrons throughout the slab.

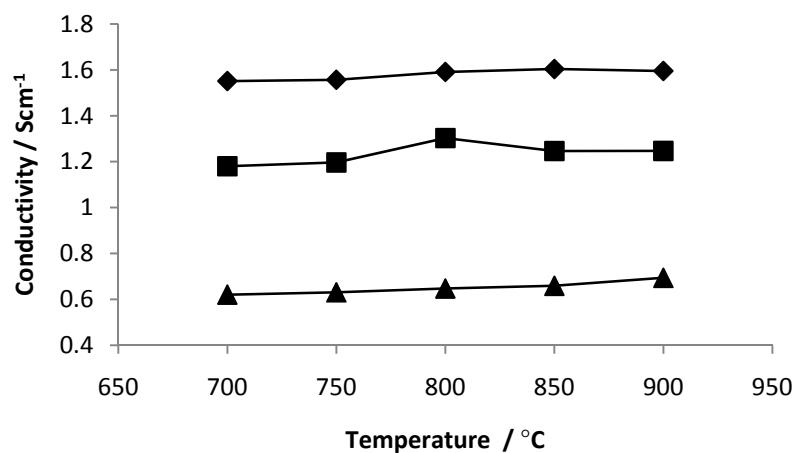


Figure 4.10 Conductivity data of various compositions of $\text{La}_{0.7}\text{Sr}_{0.3}\text{V}_x\text{O}_3$, $x = 1.0$ (diamonds), $x = 0.95$ (squares), $x = 0.9$ (triangles).

4.4 Conclusions

This research has shown that LSV is a suitable electron conductor for SOFCs. It has been identified that Sr doping concentrations of $x = 0.4$ and below result in single phase electron conducting oxides after reduction and after redox cycles. $\text{La}_{0.7}\text{Sr}_{0.3}\text{VO}_3$ has demonstrated suitable conductivity as a bulk solid and when infiltrated into a porous slab. BET isotherm confirmed that larger surface areas are created when calcinations occurs at 973 K than 1173 K. Fuel cell tests confirmed that the addition of a catalyst is required for LSV to obtain good performance in both humidified H_2 and CH_4 .

A loss of performance was observed when calcinations in air at 973 K occurred after the Pd was added to the LSV anode. This performance loss was decreased by creating a vanadium deficient LSV, suggesting that the vanadium is negatively interacting with the Pd. It was shown that vanadium deficiencies greater than 0.10 deficient are not single phase due to the formation of an La_2O_3 impurity phase. Data suggests that greater vanadium deficiencies past 0.05 deficient also result in reduced electron conductivity.

4.5 Future Work

Future work should concentrate on continuing to explore vanadium deficient LSV. Experiments should be directed toward discovering if other catalysts such as Cu or CeO₂ also interact poorly with LSV and require vanadium deficient LSV to achieve better performance. This could be done by making fuel cells infiltrated with identical loadings of vanadium deficient LSV and then selectively adding various catalysts and comparing performance.

4.6 References

1. Ge, X.; Chan, S.; Lanthanum Strontium Vanadate as Potential Anodes for Solid Oxide Fuel Cells. *Journal of Electrochemical Society*. **2009**, 156, B386-B391.
2. Cheng, Z.; Zha, S.; Aguilar, L.; Liu, M. Chemical, Electrical, and Thermal Properties of Strontium Doped Lanthanum Vanadate. *Solid State Ionics*. **2005**, 176, 1921-1928.
3. Corre, G.; Kim, G.; Cassidy, M.; Vohs, J.; Gorte, R.; Irvine, J. Activation and Ripening of Impregnated Manganese Containing Perovskite SOFC Electrodes Under Redox Cycling. *Chemistry of Materials*. **2009**, 21, 1077-1084.
4. Hui, S.; Petric, A.; Conductivity and Stability of SrVO₃ and Mixed Perovskites at Low Oxygen Partial Pressures. *Solid State Ionics*. **2001**, 143, 275-283.
5. Park, J. S.; Hasson, I. D.; Gross, M. D.; Chen, C.; Vohs, J. M.; Gorte, R. J. A High Performance Solid Oxide Fuel Cell Anode Based on Lanthanum Strontium Vanadate. Submitted to *Journal of Electrochemistry*. [Under Review]
6. Korn, M.G.A.; Santos, D.S.S.; Welz, B.; Vale, M.G.R.; Teixeira, A.P.; Lima, D.C.; Ferreira, S.L.C. Atomic Spectrometric Methods for the Determination of Metals and Metalloids in Automotive Fuels-A review. *Talanta* **2007**, 73, 1-11.